Dynamics of Single-Axle Rail Wheelsets Incorporating Profiled Wheels and Rails

Matthew McFarlane

Supervisor: Dr. Meilan Liu

A thesis submitted to the Faculty of Graduate Studies

in partial fulfillment of the requirements for the

Master of Science in Engineering Degree in

Control Engineering

Lakehead University

August 2009

Abstract

This thesis presents the theories and numerical simulations in regard to the behaviour of a single-axle railway wheelset commonly used in cargo rail cars. Specifically, creep forces, dynamic models, real wheel-rail profiles, and multiple point contact will be investigated.

One of the most important aspects of wheel-rail interactions is the creep force. Creep force results from the relative motion between the wheel and rail. The extent of such relative motion is measured by creepage, which is defined as the difference between ideal, or pure rolling, where the velocities of the wheel and rail relative to one another are equal, and the deviation of such. Creep force is an important design factor in relation to rail transport safety and efficiency as well as wheel and rail longevity.

Calculation of the dynamic creep forces will be completed with a nine-step process and benchmarked against Polach and Kalker. The Polach benchmarking tests three sets of creepage combinations proposed by Polach. In this test, a total of fifteen cases are tested. The relative accuracy and computational efficiency amongst the theories is determined. The creep forces are then plotted with respect to specific track cases and compared with multiple theories including Kalker's FASTSIM results.

Three dynamic models will then be presented, and compared. These models will be tested under specific track conditions from the Manchester Benchmarks' Track Case 2 (TC2). These models will be compared in the response, the time to calculate and the flexibility of the model to withstand parameter deviations.

Real wheel and rail profiles will then be introduced to replace the coned wheels and knife-edge rail assumption in one final model. This model makes neither small angle assumptions nor normal force assumptions. Contact conditions will include one-point contact, at either the tread or the flange, as well as two-point tread-flange contact. This model will be tested again with TC2. Hunting, a side-to-side movement at specific velocities, will be investigated.

Mechanical passive control will then be examined. The Modified-Garg model and Model I will both make use of two springs; a yaw spring, and a lateral spring. The yaw spring will be tested over a wide range of values and the distance for the system to settle to 5% of the original displacement will be investigated.

The thesis concludes with some recommendations for future work.

Acknowledgements

I would like to thank my supervisor, Dr. Meilan Liu for her outstanding support and patient guidance. Her willingness to discuss new topics and challenges was an invaluable part of my studies. I would also like to thank Dr. Hao Bai for being my co-supervisor. Appreciation to the examiners; Dr. Kefu Liu and Dr. Sultan Siddiqui for their time and effort reviewing my work, their additional input, and helping me finalize the details. Lastly, I thank my wife, Erin, for her patience and unending support.

This work was partially supported by my advisor through a Discovery Grant funded by the Natural Sciences and Engineering Research Council (NSERC) of Canada.

Table of Contents

List of Tables

List of Figures

List of Appendices

Chapter 1 – Introduction

1.1 Introduction

The history of rail going vehicles dates back to 18th century Europe with wooden wagon-ways with horse-drawn carts. These evolved into steel railed wagon-ways, then tram-ways, and on to steam power, and the steam locomotive. The growth of the rail and transportation networks facilitated the industrial revolution.

Rail transport today is a very important part of the transportation network. All over the world it is used to move both goods, specifically heavy goods, as well as people across the continents.

Railway dynamics have been of interest for practical application for many decades. Dynamic stability was being researched as early as the 1960's [1.1, 1.2], and research into practical wheel-rail contact blossomed in the 1970's [1.3].

At the core of railway dynamics is the wheel-rail contact. Many theories attempt to define and calculate this contact point or area. This thesis investigates this contact area and its effect.

1.2 Objective

The author will propose a wheelset dynamic model consisting of a rigid axle with two profiled wheels operating on canted rails. The model will be able to address track changes and disturbances, side-to-side movement or hunting, and natural damping in order to increase safety and efficiency. The model will be flexible in order to provide an excellent base for tests and experiments.

1.3 Organization

This thesis contains 6 chapters.

Chapter 1 provides the introduction. Chapter 2 presents a literature review into railway dynamics. Chapter 3 presents several wheel-rail interaction theories that determine creepages and the forces that they provide. These creep theories include; Johnson and Vemeulen's nonlinear, Kalker's linear, Heuristic nonlinear, and Polach nonlinear.

Chapter 4 is concerned with the benchmarking of the creep forces. Two static benchmarking cases will be presented. The first, the Polach benchmarking, is performed to ensure a correct interpretation of the Polach theory. The second, the Five Theories Benchmarking, compares the Johnson and Vermeulen, Kalker linear, FASTIM, Polach and Heuristic theories against one another in both output and computation time. The second part of the chapter is devoted to dynamic benchmarking. Three models will be

presented and tested with specific parameters and a predetermined track case. The responses of these three models will be compared.

Chapter 5 derives a final model. This Modified-Garg model incorporates the use of profiled wheels and rails, makes neither small angle assumptions nor normal force assumptions. It uses track-dependant creep forces, calculates normal forces, and positions of contact points at ever step. Contact conditions will include one-point on the tread or on the flange, and two-point (flange and tread). This model will be compared to Model I from Chapter 4, in both a track disturbance test as well as a test to find a critical speed. Lastly, this model will be used for an investigation into mechanical passive control.

Chapter 6 provides a conclusion and recommendations for future work.

Chapter 2 – Literature Review

2.1 Railway Dynamics

Railway vehicles were first used in the 18th century, but it was not until the 20th century that engineers began to understand their dynamics [2.1].

In 2001, Shabana and Sany published a comprehensive survey on rail vehicle simulations [2.2]. Reference [2.2] devoted an entire section to the issue of wheel-rail contact, also known as wheel-rail interaction. This clearly showed the importance of such an interaction. The accurate calculation of the interaction forces is involved with, but not limited to, a few aspects such as proper definition of creepages, rigid versus elastic contact, and contact theories. A brief review of these aspects will be given in the next section. It is worth mentioning that the wheel-rail interaction [2.2] "has a significant effect on the vehicle dynamics and stability." Here, the stability included hunting, twist and roll, pitch and bounce, and so on. This thesis focuses on lateral dynamics and lateral instability, or hunting. A review on hunting will be given in Section 2.3.

2.2 Wheel-Rail Interaction

In the case of railway dynamics, the wheel and rail are considered two rigid bodies that are in contact at a point. If either of these bodies rotate or translate relative to the other, the contact point will also shift. The resulting velocities of each body at the contact point may not be equal.

When the velocities are equal, the bodies are said to be undergoing 'pure rolling'. When the velocities are not equal there is said to be creepage. Creepage is a term defining the deviation of the actual rolling condition between two rigid bodies from pure rolling. Creepage can be defined in both the lateral and longitudinal directions as well as about the common normal.

The relationship between creepage and creep forces was first offered by Carter in 1926. Carter proposed an exact closed-form solution for the relationship between longitudinal and tangential force [2.3]. Carter's analysis was based on a cylinder rolling on a plane, which only considers force in the rolling direction. This alone is not sufficient for the calculation of railway dynamics [2.4].

In 1964, Johnson and Vermeulen extended Carter's work of arbitrary smooth half-spaces to pure creepage without spin. Johnson and Vermeulen used Hertz theory to calculate shape and size of the wheel-rail contact area. They included an elliptical contact area as well as stated that the ratio of the semi-axes of the ellipse is a function of the curvature of the wheel and the railhead [2.3].

Kalker developed his linear theory [2.5] suggesting that for very small creepages, the area of slip is very small and its effect can be neglected. Therefore the adhesion area is assumed to be equal to the contact area. As a result a linear relation is used between the

creepages and the creep forces and moment. Kalker proceeded to write his exact theory [2.6] which was not limited to very small creepages.

In 1979, Kalker wrote a program called DUVOROL. DUVOROL calculated the contact forces between two rolling bodies with identical elastic constants that have contact according to the Hertz theory. DUVOROL was used by British Rail to construct a book of tables in support of vehicle simulation [2.4].

Kalker continued to write CONTACT (1982, [2.7]), a program that allowed for the calculation of creep forces using Kalker's exact theory. Kalker, comparing with Johnson and Vermeulen's experimental data, found an error of less then five to ten percent [2.8, 2.9].

Both DUVOROL and CONTACT are based on Kalker's exact theory, and therefore require considerable computation time. They are not well-suited to real-time calculations. Kalker then introduced his simplified theory in 1973 [2.10] which he used to write FASTSIM [2.11]. FASTSIM was found to be 400 times faster then CONTACT [2.2].

Shen et. al. improved the Johnson and Vermeulen theory by incorporating Kalker's exact linear theory's calculation of spin. This model became known as the Heuristic model or Shen-Hedrick-Elkins theory [2.9]

Lastly, Polach's model [2.12] is claimed to performed better under high creepage than Kalker, although it is based on his work with simplification of the distribution of normal and tangential stresses in the wheel-rail contact patch. This theory can calculate the creep forces efficiently and effectively with reduced computational effort [2.6]. Polach also extended his creep force model for large creep applications by introducing reduction factors for the Kalker coefficients to differentiate the areas of adhesion and slip [2.4].

More recent research in regard to wheel-rail interactions considers wheel and rail elastic and dissipating energy [2.13 – 2.15]. For example, the Hertz contact force model proposed in [2.14-2.15] accounts for indentation (penetration) and energy dissipation (hysteresis damping).

2.3 Hunting

Hunting refers to the self-excited lateral-yaw oscillation of the wheelset, see Figure 2.1 [2.1]. It is self-excited, because it takes place when the vehicle speed reaches and surpasses a certain speed, known as the critical speed. Once the oscillation is self-excited, the wheelset sways from side to side. This sway causes the wheelset to rotate about the vertical axis as depicted in Figure 2.1.

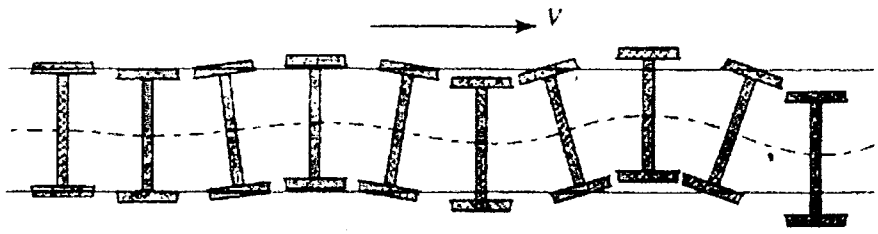

Figure 2.1 – Hunting

Hunting phenomenon is believed to be first observed as early as 1821 [2.1], although it was not well understood until a number of decades later. A brief review in [2.16] suggests that advanced study of the hunting problem started in the 1960's [2.17-2.18]. By the 1990's hunting was examined in the light of bifurcation of nonlinear systems [2.19-2.21].

The practical importance of hunting lies in the fact [2.16] that it can cause wear to the wheels and rails. It can cause bogie hunting, which can lead to rail car body hunting. The large lateral force occurring during hunting can lead to derailment.

Chapter 3 - Determination of Creep Forces

3.1 Introduction to Creep

When two rigid bodies move relative to one another as in the wheel-rail interaction the contact point will continually shift from the original position. The resulting velocities of the two bodies at the contact point may or may not equal. This interaction includes two forces; the normal force and the creep force. The creep force is the difference between pure rolling, where these two velocities are equal, and the actual condition. The creep force is also known as the dry frictional force while creepage is the relative motion. Creepage in the wheel-rail interaction is defined laterally, longitudinally and about the common normal to the contact point, or the spin creepage. Note that creep forces can be both positive and negative.

3.2 Overview of Various Creep Theories

There are a number of theories to calculate creepage and creep. In this thesis, five theories will be considered; Johnson and Vermeulen's nonlinear, Kalker's linear and nonlinear, Heuristic nonlinear and Polach nonlinear.

Several preliminary calculations must be completed prior to the calculation of creep using the above theories.

The first part of the preliminary calculations involves factors K_1, K_2, K_3, and K_4. Factors K_1 and K_2 both depend on the material properties of the wheel and rail [3.1].

$$K_1 = \frac{1-\upsilon_w^2}{\pi E} \tag{3.1}$$

$$K_2 = \frac{1-\upsilon_r^2}{\pi E} \tag{3.2}$$

where E is the modulus of elasticity, and υ is the Poisson's ratio. The subscripts w and r mean the wheel and rail respectively. Factors K_3 and K_4 [3.1] depend on the geometrical properties of the wheel and rail.

$$K_3 = \frac{1}{2}\left(\frac{1}{R_1^r} + \frac{1}{R_2^r} + \frac{1}{R_1^w} + \frac{1}{R_2^w}\right) \tag{3.3}$$

$$K_4 = \frac{1}{2}\left[\left(\frac{1}{R_1^w} + \frac{1}{R_2^w}\right)^2 + \left(\frac{1}{R_1^r} + \frac{1}{R_2^r}\right)^2 + 2\left(\frac{1}{R_1^w} - \frac{1}{R_2^w}\right)\left(\frac{1}{R_1^r} - \frac{1}{R_2^r}\right)\cos 2\psi\right]^{\frac{1}{2}} \tag{3.4}$$

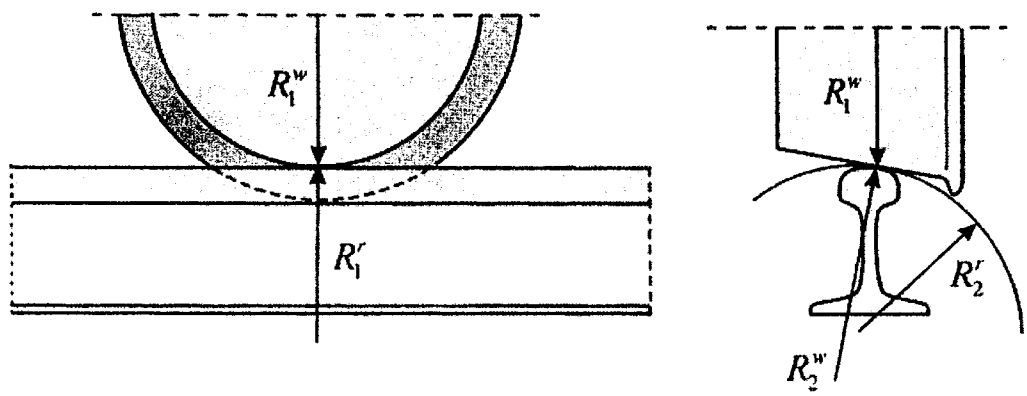

Figure 3.1 – Principal Radii of Wheel and Rail [3.1]

For the case of conical wheels (see Figure 3.1) R_1^w is the wheel radius, $R_2^w = \infty$ for the radius of wheel cone, $R_1^r = \infty$ for the longitudinal radius of the track and R_2^w is the rail profile radius. Angle ψ describes the yaw angle of the wheelset (which is the rotation about the vertical axis).

Once the K_i (i=1,...,4) factors are determined, Hertz coefficients m and n will be interpolated for in computer calculation as follows [3.1]:

$$m = A_m \tan(\theta - \frac{\pi}{2}) + \frac{B_m}{\theta^{C_m}} + D_m \tag{3.5}$$

$$n = \frac{1}{A_n \tan(\theta - \frac{\pi}{2}) + 1} + B_n \theta^{C_n} + D_n \sin\theta \tag{3.6}$$

where θ is:

$$\theta = \cos^{-1}\left(\frac{K_4}{K_3}\right) \tag{3.7}$$

and coefficients A_k, B_k, C_k, and D_k ($k = m, n$) are given in Table 3.1 [3.1]. The values in Table 3.1 are carried to twelve significant digits due to the consideration that they greatly affect the preliminary calculations.

Table 3.1 – Values of A_k, B_k, C_k, and D_k

A_m	-1.086419052477	A_n	-0.773444080706
B_m	-0.106496432832	B_n	0.256695354565
C_m	1.350000000000	C_n	0.200000000000
D_m	1.057885958251	D_n	-0.280958376499

The semi-axes of the contact ellipse are then determined by:

$$a = m\left[\frac{3\pi N(K_1 + K_2)}{4K_3}\right]^{\frac{1}{3}} \tag{3.8}$$

$$b = n\left[\frac{3\pi N(K_1 + K_2)}{4K_3}\right]^{\frac{1}{3}} \tag{3.9}$$

with N being the normal force acting on the contact ellipse.

The second part of the preliminary calculations evaluates creepages, defined as [3.1]:

$$\zeta_x = \frac{\left(\dot{r}_p^w\right)\cdot t_1^r}{V} \tag{3.10}$$

$$\zeta_y = \frac{\left(\dot{r}_p^w\right)\cdot t_2^r}{V} \tag{3.11}$$

$$\varphi = \frac{\left(\omega^w\right)\cdot n^r}{V} \tag{3.12}$$

where $\dot{r}_p^w$ is the velocity vector of the wheel at the contact point with respect to the global coordinate system, V is the forward speed and t_1^r, t_2^r, and n^r are the base unit vectors (Figure 3.2), ω^w is the angular velocity vector of the wheel with respect to the global coordinate system ($\omega^w = A^w\bar{\omega}^w$, with $\bar{\omega}^w$ defined by (3.15) and A^w by (3.17), see discussions below). The velocity vector $\dot{r}_p^w$ is determined by,

$$\dot{r}_p^w = \dot{R}^w + A^w(\bar{\omega}^w \times \bar{U}_p^w) \tag{3.13}$$

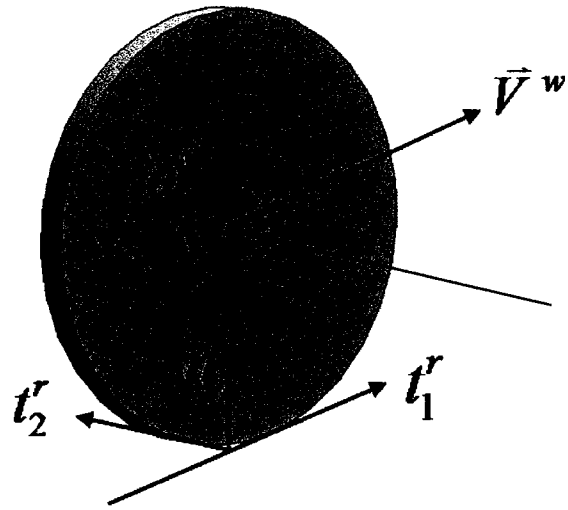

Figure 3.2 – Contact Frame [3.1]

where R^w is the global position vector of the origin of the wheelset coordinate system:

$$R^w = \begin{bmatrix} R_x^w \\ R_y^w \\ R_z^w \end{bmatrix} \tag{3.14}$$

The $\bar{\omega}^w$ in (3.13) is the angular velocity vector of the wheel with respect to the wheelset coordinate system:

$$\bar{\omega}^w = \begin{bmatrix} \bar{\omega}_x^w \\ \bar{\omega}_y^w \\ \bar{\omega}_z^w \end{bmatrix} \tag{3.15}$$

and $\overline{U}_p^w$ is the local position vector of the wheel contact point with respect to the wheelset coordinate system:

$$\overline{U}_p^w = \begin{bmatrix} 0 \\ \mp g_a / 2 \\ -r_0 \end{bmatrix} \tag{3.16}$$

where r_0 is the wheel rolling radius and g_a is the track gauge. The upper negative signs are used with the right wheel, while the lower positive signs are used with the left wheel. The A^w matrix in (3.13) defines the orientation of the wheelset with respect to the global coordinate system. The rotations are as follows: ψ^w is a rotation about the Z^w axis or the yaw, ϕ^w is a rotation about the X^w axis or the roll and θ^w is a rotation about the Y^w axis or the pitch.

$$A^w = \begin{bmatrix} \cos\psi^w \cos\theta^w - \sin\psi^w \sin\phi^w \sin\theta^w & -\sin\psi^w \cos\phi^w & \cos\psi^w \sin\theta^w + \sin\psi^w \sin\phi^w \cos\theta^w \\ \sin\psi^w \cos\theta^w + \cos\psi^w \sin\phi^w \sin\theta^w & \cos\psi^w \cos\phi^w & \sin\psi^w \sin\theta^w - \cos\psi^w \sin\phi^w \cos\theta^w \\ -\cos\phi^w \sin\theta^w & \sin\phi^w & \cos\phi^w \cos\theta^w \end{bmatrix} \tag{3.17}$$

The base unit vectors in (3.10) – (3.12) are:

$$\begin{bmatrix} t_1^r & t_2^r & n^r \end{bmatrix} = A^w \begin{bmatrix} 1 & 0 & 0 \\ 0 & \cos\delta_r & \pm\sin\delta_r \\ 0 & \mp\sin\delta_r & \cos\delta_r \end{bmatrix} \tag{3.18}$$

where δ_r is the contact angle between the lateral tangent and the wheelset (see Figure 3.3). Again, where there are $\pm$ or $\mp$ signs, the upper sign is to be used for the right wheel, while the lower is to be used with the left.

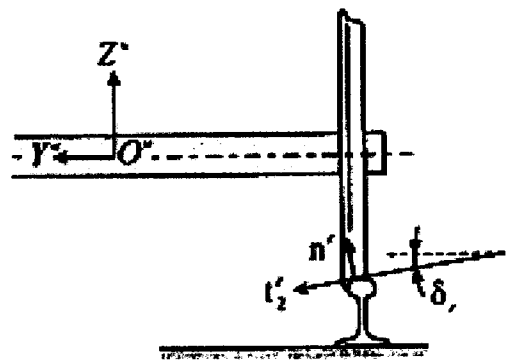

Figure 3.3 – Wheelset Frame [3.1]

Once the creepages ζ_x and ζ_y are determined, they are then used to find normalized creepages ζ and η, and the normalized resultant creepage τ [3.1].

$$\zeta = \frac{\pi abG}{\mu N}\frac{\zeta_x}{\phi_1} \tag{3.19}$$

$$\eta = \frac{\pi abG}{\mu N}\frac{\zeta_y}{\psi_1} \tag{3.20}$$

$$\tau = \sqrt{\zeta^2 + \eta^2} \tag{3.21}$$

where G is the combined modulus of elasticity, μ is the coefficient of friction, and N is the normal force. The parameters ϕ_1 and ψ_1 are,

$$\left.\begin{aligned} \phi_1 &= \left(\frac{b}{a}\right)\left[D_e - \upsilon\left(D_e - C_e\right)\right] \\ \psi_1 &= \left(\frac{b}{a}\right)\left[D_e - \upsilon C_e\right] \end{aligned}\right\} \quad \text{for } a \geq b, \quad e = \sqrt{1 - \left(\frac{b}{a}\right)^2} \tag{3.22a}$$

or,

$$\left.\begin{aligned} \phi_1 &= B_e - \upsilon(D_e - C_e) \\ \psi_1 &= B_e - \upsilon\left(\frac{a}{b}\right)^2 C_e \end{aligned}\right\} \quad \text{for } a \leq b, \quad e = \sqrt{1 - \left(\frac{a}{b}\right)^2} \tag{3.22b}$$

In the above equation υ is the Poisson's ratio, and B_e, C_e, and D_e, are in terms of elliptical integrals of argument e.

$$B_e = K(e) + \frac{E(e) - K(e)}{e^2} \tag{3.23}$$

$$C_e = \frac{K(e) - E(e)}{e^2} \tag{3.24}$$

$$D_e = \frac{2}{3}\left[\frac{-K(e)+E(e)}{e^4} + \frac{K(e)-\frac{1}{2}E(e)}{e^2}\right] \tag{3.25}$$

with *K(e)* being the complete elliptical integral of the first kind, and *E(e)* the complete elliptical integral of the second kind.

3.3 Johnson and Vermeulen's Nonlinear Theory

A brief summary of early work on contact and creep forces is first given. In 1882, the Hertz contact theory was proposed. In this theory, the area of contact was assumed elliptical. The theory accounts for the shape of the surfaces in the region of the contact area.

Carter in 1926 introduced the first two-dimensional creep theory. The theory recognized that creepage is due to a combination of friction and elastic deformation. In 1958, Johnson extended Carter's work to three-dimensional space with two spheres neglecting spin. Six years later, Johnson and Vermeulen further extended the method to smooth half-spaces without spin. "In this theory, the contact surface between the two rolling bodies transmitting a tangential force is asymmetrically divided into two regions: the slip region and the stick or no-slip region. The adhesion area was assumed to be elliptical. The area of adhesion is assumed to touch the leading edge of the contact ellipse" [3.1], see Figure 3.4.

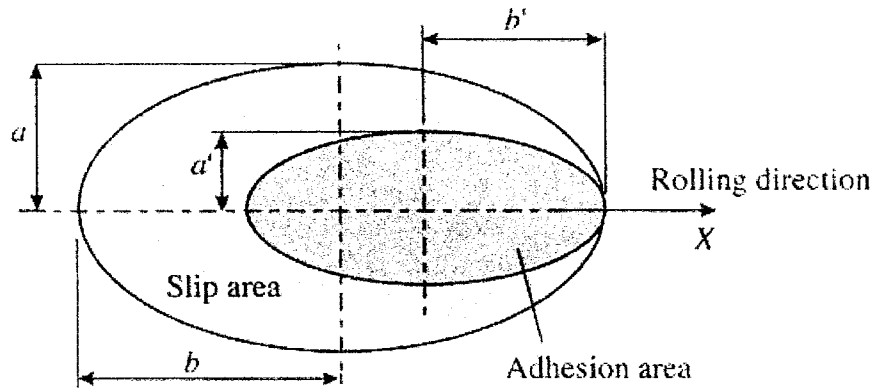

Figure 3.4 – Contact Ellipse, Adhesion and Slip Areas [3.1]

The vector creep force is,

$$\mathbf{F} = -\left(\frac{\mu N}{\tau}\right)\begin{cases}\left[1-\left(1-\frac{\tau}{3}\right)^2\right](\zeta\mathbf{i}+\eta\mathbf{j}), & |\tau| \le 3 \\ (\zeta\mathbf{i}+\eta\mathbf{j}), & |\tau| > 3\end{cases} \tag{3.26}$$

where ζ, η and τ have been defined in (3.19) – (3.21). The unit vectors **i** and **j** represent the directions of the longitudinal and lateral creep.

Although the Johnson and Vermeulen theory does not calculate for spin, it adopts the saturation law. It is therefore appropriate for cases of large longitudinal or lateral creepage without spin. The application of this theory is somewhat limited due to the longer computation time required by the elliptical integrals, and due to the exclusion of spin effect.

3.4 Kalker's Theories

Kalker suggested that for very small creepages, the area of slip is very small and its effect can be neglected. Therefore, the adhesion area can be assumed to be equal to the contact area. As a result, the linear relation between creepages and creep forces including the moment is,

$$\begin{bmatrix} F_x \\ F_y \\ M \end{bmatrix} = -Gab \begin{bmatrix} c_{11} & 0 & 0 \\ 0 & c_{22} & \sqrt{ab}c_{23} \\ 0 & -\sqrt{ab}c_{23} & abc_{33} \end{bmatrix} \begin{bmatrix} \zeta_x \\ \zeta_y \\ \varphi \end{bmatrix} \tag{3.27}$$

where G is the combined modulus of rigidity, and c_{ij} are the creepage and spin coefficients (also known as Kalker's linear coefficients) and depend only on Poisson's ratio and the ratio of the semi-axes of the contact ellipse (a and b). The coefficients are given in Table 3.2. These coefficients were calculated by Kalker, assuming small slip and a contact area that was not necessarily elliptical. With regard to the validity of the coefficients given in Table 3.2, Kalker conducted an extensive calculation. It was determined that these coefficients had an error of less than five percent [3.1].

In addition to the linear theory, Kalker made significant contributions to the field of wheel-rail contact. For example, based on his three-dimensional rolling contact theory, he authored the now well known computer program CONTACT [3.2]. Since CONTACT did not compute quickly enough to meet the demand of railway dynamic simulations, a series of tables (known as USETAB) were pre-calculated and made available for interpolation in railway vehicle dynamic simulation [3.3]. Kalker continued to develop a simplified

theory in which the tangential traction-displacement relation takes a simple linear form [3.4]. By 1982, Kalker authored another well known computer program called FASTSIM based on his simplified theory [3.5]. Kalker's linear theory and the FASTSIM program are widely used in railroad vehicle dynamics, but the linear theory is limited to cases of small creepages [3.1]. His exact theory (3D and nonlinear) in the form of lookup tables is also used in some railway system dynamic simulation packages such as DYNARAIL (by Center for Automated Mechanics, U.S. DOT), NUCARS (by Transportation Technology Center Inc, a subsidiary of the Association of American Railroads), and VAMPIRE (by DeltaRail Group, Ltd., U.K.)

Table 3.2 – Coefficients Used in Kalker Theory

Kalker's Creepage and Spin Coefficients

	c_{11}			c_{22}			$c_{23} = -c_{32}$			c_{11}		
g	$\nu = 0$	0.25	0.5	$\nu = 0$	0.25	0.5	$\nu = 0$	0.25	0.5	$\nu = 0$	0.25	0.5
(a/b)												
0.1	2.51	3.31	4.85	2.51	2.52	2.53	0.334	0.473	0.731	6.42	8.28	11.7
0.2	2.59	3.37	4.81	2.59	2.63	2.66	0.483	0.603	0.809	3.46	4.27	5.66
0.3	2.68	3.44	4.8	2.68	2.75	2.81	0.607	0.715	0.889	2.49	2.96	3.72
0.4	2.78	3.53	4.82	2.78	2.88	2.98	0.720	0.823	0.977	2.02	2.32	2.77
0.5	2.88	3.62	4.83	2.88	3.01	3.14	0.827	0.929	1.07	1.74	1.93	2.22
0.6	2.98	6.72	4.91	2.98	3.14	33.1	0.930	1.03	1.18	1.56	1.68	1.86
0.7	3.09	3.81	4.97	3.09	3.28	3.48	1.03	1.14	1.29	1.43	1.50	1.60
0.8	3.19	3.91	5.05	3.19	3.41	3.65	1.13	1.25	1.40	1.34	1.37	1.42
0.9	3.29	4.01	5.12	3.29	3.54	3.82	1.23	1.36	1.51	1.27	1.27	1.27
(b/a)												
1.0	3.4	4.12	5.2	3.40	3.67	3.98	1.33	1.47	1.63	1.21	1.19	1.16
0.9	3.51	4.22	5.3	3.51	3.81	4.16	1.44	1.57	1.77	1.16	1.11	1.06
0.8	3.65	4.36	5.42	3.65	3.99	4.39	1.58	1.75	1.94	1.10	1.04	0.954
0.7	3.82	4.54	5.58	3.82	4.21	4.67	1.76	1.95	2.18	1.05	0.965	0.852
0.6	4.06	4.78	5.8	4.06	4.50	5.04	2.01	2.23	2.50	1.01	0.892	0.751
0.5	4.37	5.10	6.11	4.37	4.90	5.56	2.35	2.62	2.96	0.958	0.819	0.650
0.4	4.84	5.57	6.57	4.84	5.48	6.31	2.88	3.24	3.70	0.912	0.747	0.549
0.3	5.57	6.34	7.34	5.57	6.40	7.51	3.79	4.32	5.01	0.868	0.674	0.446
0.2	6.96	7.78	8.82	6.96	8.14	9.79	5.72	6.63	7.89	0.828	0.601	0.341
0.1	10.7	11.7	12.9	10.7	12.8	16.0	12.2	14.6	18.0	0.795	0.526	0.228

Note: $g = 0$, $c_{11} = \pi^2/4(1 - \nu)$; $c_{22} = \pi^2/4$; $c_{23} = -c_{32} = \pi\sqrt{g}\,[1 + \nu(0.5\Lambda + \ln 4 - 5)]/3(1 - \nu)$; $\Lambda = \ln(16/g^2)$; and $c_{11} = \pi^2/16(1 - \nu)g$.

Source: Kalker, J.J., *Three-Dimensional Elastic Bodies in Rolling Contact*, Kluwer, Dordrecht, Netherlands, 1990. With permission.

While commercial packages typically interpolate the tabulated results, the present study employs curve-fitted results in order to reduce calculation time. For a Poisson's ratio of $\upsilon = 0.28$ the creepage and spin coefficients can be curve fitted by the Datafit [3.6] software as follows,

$$c_{11} = 3.3914 + \frac{0.69827}{\left(\frac{b}{a}\right)} + \frac{0.21286}{\left(\frac{b}{a}\right)^2} - \frac{7.4786\times10^{-2}}{\left(\frac{b}{a}\right)^3} + \frac{1.0671\times10^{-2}}{\left(\frac{b}{a}\right)^4} - \frac{5.1743\times10^{-4}}{\left(\frac{b}{a}\right)^5} \tag{3.28}$$

$$c_{22} = 2.3753 + \frac{1.2885}{\left(\frac{b}{a}\right)} + \frac{8.0730\times10^{-2}}{\left(\frac{b}{a}\right)^2} - \frac{5.1449\times10^{-2}}{\left(\frac{b}{a}\right)^3} + \frac{8.4577\times10^{-3}}{\left(\frac{b}{a}\right)^4} - \frac{4.3277\times10^{-4}}{\left(\frac{b}{a}\right)^5} \tag{3.29}$$

$$c_{23} = 0.40890 + \frac{1.0652}{\left(\frac{b}{a}\right)} - \frac{4.6576\times10^{-3}}{\left(\frac{b}{a}\right)^2} + \frac{2.5407\times10^{-2}}{\left(\frac{b}{a}\right)^3} - \frac{4.3437\times10^{-3}}{\left(\frac{b}{a}\right)^4} + \frac{2.2442\times10^{-4}}{\left(\frac{b}{a}\right)^5} \tag{3.30}$$

$$c_{33} = 0.41960 + \frac{0.74933}{\left(\frac{b}{a}\right)} - \frac{1.3928\times10^{-2}}{\left(\frac{b}{a}\right)^2} - \frac{6.1529\times10^{-4}}{\left(\frac{b}{a}\right)^3} \tag{3.31}$$

Finally, it is to be noted that, in this thesis, both the Kalker linear theory and FASTSIM will be used. FASTSIM incorporates the saturation law, and is therefore applicable to the case of large creepage and spin.

3.5 Heuristic Nonlinear Theory

The Heuristic theory [3.1] begins with the calculation of the longitudinal and lateral creep forces F_x^k and F_y^k using Kalker's linear theory.

$$\begin{bmatrix} F_x^k \\ F_y^k \end{bmatrix} = -Gab \begin{bmatrix} c_{11} & 0 & 0 \\ 0 & c_{22} & \sqrt{abc_{23}} \end{bmatrix} \begin{bmatrix} \zeta_x \\ \zeta_y \\ \varphi \end{bmatrix} \tag{3.32}$$

The resultant creep force is evaluated:

$$\overline{F}_L = \sqrt{\left(F_x^k\right)^2 + \left(F_y^k\right)^2} \tag{3.33}$$

and the saturation law applied:

$$F_L = \begin{cases} \mu N \left[\left(\dfrac{\overline{F}_L}{\mu N} \right) - \dfrac{1}{3} \left(\dfrac{\overline{F}_L}{\mu N} \right)^2 + \dfrac{1}{27} \left(\dfrac{\overline{F}_L}{\mu N} \right)^3 \right], & \overline{F}_L \le 3\mu N \\ \mu N, & \overline{F}_L > 3\mu N \end{cases} \tag{3.34}$$

The creep–force reduction coefficient is defined:

$$\overline{\varepsilon} = \frac{F_L}{\overline{F}_L} \tag{3.35}$$

The nonlinear creep-forces are determined as:

$$\begin{bmatrix} F_x \\ F_y \end{bmatrix} = \overline{\varepsilon} \begin{bmatrix} F_x^k \\ F_y^k \end{bmatrix} \tag{3.36}$$

The heuristic theory produces more realistic values for creep forces outside the linear range than Kalker's linear and simplified theories. However in the case of high values of spin, the heuristic theory may lead to unsatisfactory results [3.1].

3.6 Polach Nonlinear Theory

The Polach theory [3.1] is based on the assumption that the contact area is elliptical in shape. Polach defines the maximum tangential stress at any arbitrary point using the Hertz contact theory as:

$$\tau_{\max} = \mu\sigma \tag{3.37}$$

where μ is the coefficient of friction, and is assumed to be constant across the entire contact area. The creep force due to creepage in both the lateral and longitudinal directions is given by:

$$F_p = -\frac{2\mu N}{\pi}\left(\frac{\varepsilon}{1+\varepsilon^2} + \tan^{-1}\varepsilon\right) \tag{3.38}$$

where ε is the gradient of the tangential stress in the area of adhesion. It is given as,

$$\varepsilon = \frac{1}{4}\frac{G\pi abC_h}{\mu N}v_c \tag{3.39}$$

In (3.39),

$$v_c = \sqrt{\zeta_x^2 + \zeta_{yc}^2} \tag{3.40}$$

$$\zeta_{yc} = \begin{cases} \zeta_y, & \left|\zeta_y + \varphi a\right| \le \left|\zeta_y\right| \\ \zeta_y + \varphi a, & \left|\zeta_y + \varphi a\right| > \left|\zeta_y\right| \end{cases} \tag{3.41}$$

The parameter C_h is defined as:

$$C_h = \sqrt{\left(c_{11}\frac{\zeta_x}{v}\right)^2 + \left(c_{22}\frac{\zeta_y}{v}\right)^2} \tag{3.42}$$

with

$$v = \sqrt{\zeta_x^2 + \zeta_y^2} \tag{3.43}$$

The creep force that accounts for the spin effect is given by [3.1],

$$F_{ps} = -\frac{9}{16} a\mu N K_p \left[1 + 6.3\left(1 - e^{-(a/b)}\right)\right] \tag{3.44}$$

The quantity K_p is,

$$K_p = \left|\varepsilon_y\right| \left(-\frac{\delta_p^3}{3} + \frac{\delta_p^2}{2} - \frac{1}{6} \right) + \frac{1}{3}\sqrt{\left(1 - \delta_p^2\right)^3} \tag{3.45}$$

with ε_y and δ_p being

$$\varepsilon_y = \frac{8}{3} \frac{Gb\sqrt{ab}}{\mu N} \left(\frac{c_{23}\zeta_{yc}}{1 + 6.3\left(1 - e^{-(a/b)}\right)} \right) \tag{3.46}$$

$$\delta_p = \frac{\left(\varepsilon_y\right)^2 - 1}{\left(\varepsilon_y\right)^2 + 1} \tag{3.47}$$

Finally, the creep forces are given as follows,

$$\begin{bmatrix} F_x \\ F_y \end{bmatrix} = \begin{bmatrix} F_p \dfrac{\zeta_x}{v_c} \\ F_p \dfrac{\zeta_y}{v_c} + F_{ps} \dfrac{\varphi}{v_c} \end{bmatrix} \tag{3.48}$$

Polach theory is known to yield accurate predictions of the creep forces [3.1].

3.7 Concluding Remarks

In this chapter, the preliminary calculations and several creep force theories have been presented. Before the theories can be applied to the dynamic wheelset models (see Chapter 5), they are to be benchmarked in the next chapter. Three kinds of benchmarking will be considered, static benchmarking in which fixed values of creep are used, benchmarking of track position-dependant creep and dynamic benchmarking.

Chapter 4 – Benchmarking of Creep Forces

4.1 Static Benchmarking of Creep

Two static benchmarking tests will be conducted; the Polach benchmarking, and the five-theories benchmarking. Here, static benchmarking refers to fixed values of creep.

4.1.1 Polach Benchmarking

This benchmarking is performed to ensure a correct interpretation of the Polach theory. In 1999, Polach published *Fast Wheel-Rail Forces Calculation Computer Code* [4.1] whereby the Polach theory and its Fortran implementation were presented. In the paper, $K_M = \left|\varepsilon_y\right|\left(\frac{\delta_p^3}{3} - \frac{\delta_p^2}{2} + \frac{1}{6}\right) - \frac{1}{3}\sqrt{\left(1-\delta_p^2\right)^3}$, which is the negative of the K_p of equation (3.45), was given to be used in the place of K_p; however K_p was used in the included Fortran program. In this thesis, through Polach benchmarking and other benchmarking cases, it is found that K_p should be used as in equation (3.45).

In [4.1], Polach presented three sets of input and computed data, the first with nine cases, and the second and third with three cases each, see Figure 4.1.

Using the c_{11}, c_{22}, c_{23} values from the Polach paper (see values in Figure 4.1), two different sets of values were compared: the values from Figure 4.1, and the values

determined by Matlab [4.2] implementation of the Polach theory as given in Section 3.6. Results are shown in Figures 4.2 through 4.4. Excellent agreements are seen in all individual cases. It should be noted that Cases 2 and 3 of Set A, and Case 2 of Sets B and C have a zero F_x; likewise, Cases 1 and 3 of Set A, and Case 3 of Sets B and C have zero or very small F_y.

Examples of results :
NY = 0.25, G = 8.4×10^{10} Nm^{-2}, PI = 3.14159, Q = 1×10^{5} N, F = 0.3

A = 6×10^{-3} m, B = 6×10^{-3} m, C1 = 4.12, C2 = 3.67, C3 = 1.47 :

SX = 0.004 SY = 0 OM = 0 m^{-1} FX = -26 732 N FY = 0 N	SX = 0 SY = 0.004 OM = 0 m^{-1} FX = 0 N FY = -25 872 N	SX = 0 SY = 0 OM = 0.004 m^{-1} FX = 0 N FY = -107 N
SX = 0.002 SY = 0.002 OM = 0.002 m^{-1} FX = -16 362 N FY = -16 398 N	SX = 0.004 SY = 0.006 OM = 0 m^{-1} FX = -16 098 N FY = -24 147 N	SX = 0.00005 SY = 0.004 OM = 0.008 m^{-1} FX = -321 N FY = -25 834 N
SX = -0.00005 SY = 0.004 OM = 0.008 m^{-1} FX = 321 N FY = -25 834 N	SX = -0.00005 SY = -0.004 OM = 0.8 m^{-1} FX = 323 N FY = 8 259 N	SX = 0.00005 SY = -0.004 OM = -0.008 m^{-1} FX = -321 N FY = 25 834 N

A = 7.5×10^{-3} m, B = 1.5×10^{-3} m, C1 = 7.78, C2 = 8.14, C3 = 6.63 :

SX = 0.002 SY = 0.002 OM = 0 m^{-1} FX = -12 606 N FY = -12 606 N	SX = 0 SY = 0.002 OM = 0.002 m^{-1} FX = 0 N FY = -13 954 N	SX = 0.002 SY = 0 OM = 0.002 m^{-1} FX = -13 421 N FY = -0.3 N

A = 1.5×10^{-3} m, B = 7.5×10^{-3} m, C1 = 3.37, C2 = 2.63, C3 = 0.603 :

SX = 0.002 SY = 0.002 OM = 0 m^{-1} FX = -5 549 N FY = -5 549 N	SX = 0 SY = 0.002 OM = 0.002 m^{-1} FX = 0 N FY = -4 919 N	SX = 0.002 SY = 0 OM = 0.002 m^{-1} FX = -6 254 N FY = 0 N

Figure 4.1 – Polach Test Cases [4.1]

(A, B = semi-axes of contact ellipse; C1, C2, C3 = Kalker's constants c_{11}, c_{22}, c_{23}; FX, FY = longitudinal and lateral forces; SX, SY = longitudinal and lateral creepages; OM = spin; Q = wheel load; F = coefficient of friction)

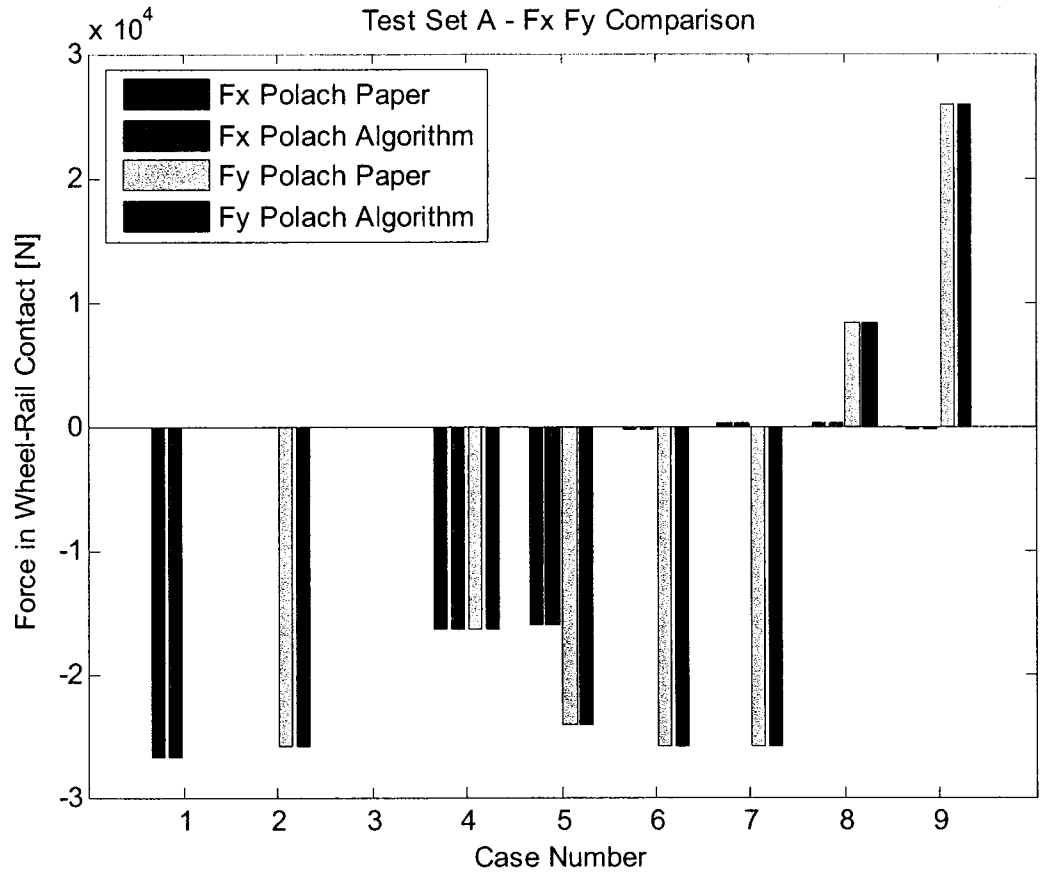

Figure 4.2 – Polach Benchmark Test Set A

(Polach Paper = values from Figure 4.1;

Polach Algorithm = values determined by Matlab implementation)

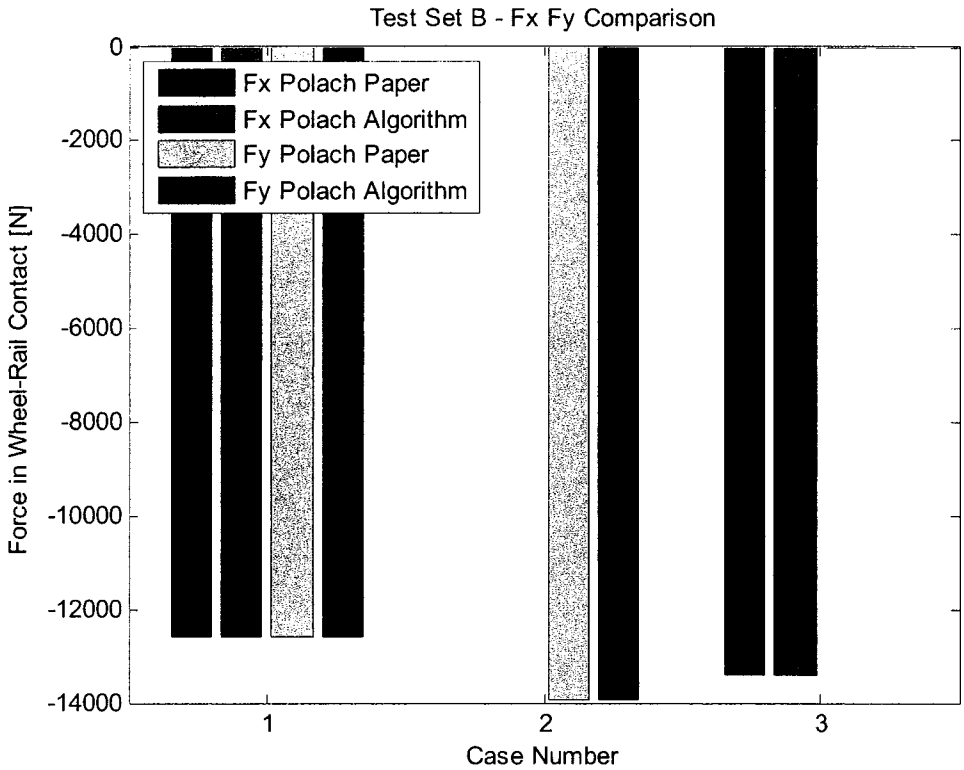

Figure 4.3 – Polach Benchmark Test Set B

(Polach Paper = values from Figure 4.1;

Polach Algorithm = values determined by Matlab implementation)

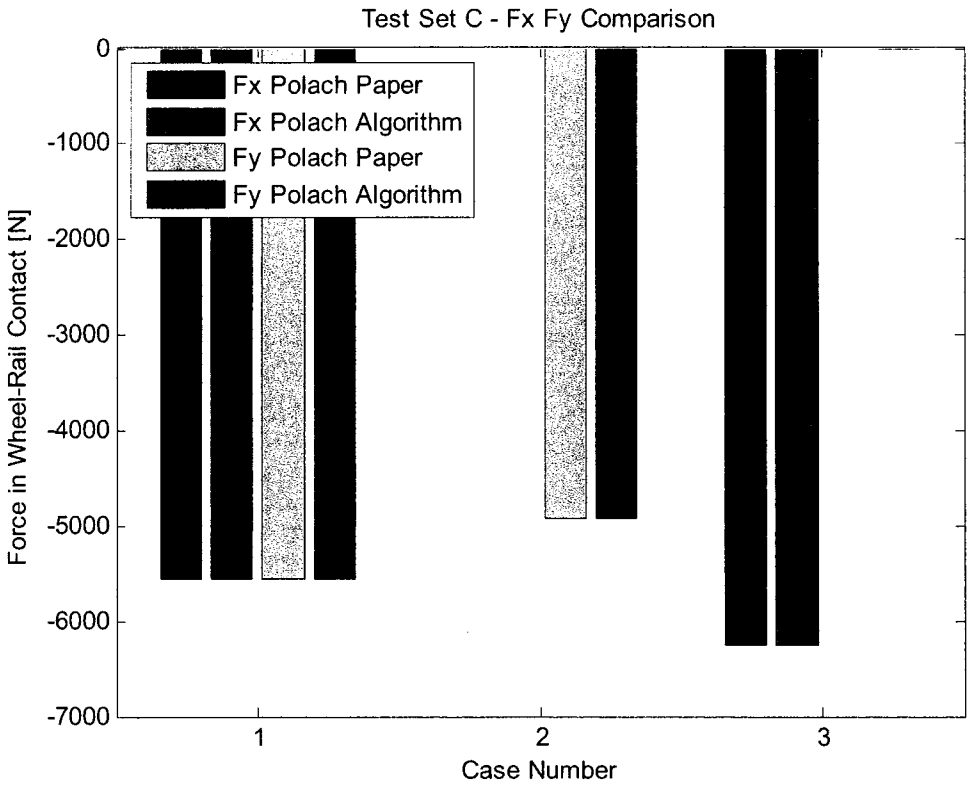

Figure 4.4 – Polach Benchmark Test Set C

(Polach Paper = values from Figure 4.1;

Polach Algorithm = values determined by Matlab implementation)

4.1.2 Five Theories Benchmarking

The five different creep theories (Johnson and Vermeulen, Kalker Linear, FASTSIM, Polach, and Heuristic) are contrasted with one another. This test is performed with the conditions given in Table 4.1. The test determines the creep forces in both the longitudinal (F_x) and lateral (F_y) directions as well as the time to complete the calculations. Results are shown in Table 4.2, and Figures 4.7 and 4.8. It is noted that the Kalker Linear theory is hence forth simply referred to as the Kalker theory.

It can be seen from Table 4.2 that the Johnson and Vermeulen, FASTSIM, Heuristic, and Polach theories all produced very similar results. The Kalker theory produced a distinctly large result. This is due to not applying the saturation law to which the other four theories are subject. A comparison of creep forces with and without the saturation law is shown in Figure 4.5. The saturation law caps the maximum value of creep force.

Table 4.1 – Parametric Values for Static Benchmarking

N_0	133,300 N
E	2.1×10^{11} N/m^2
G	8×10^{8} N/m^2
μ	0.15
υ	0.28
R_1^w	0.457 m
R_2^r	0.254 m
V	20 m/s

Table 4.2 – Creep Forces by Various Theories

	Fx [N]	Fy [N]
Johnson and Vermeulen	1.9995×10^{4}	1.9064×10^{-4}
Kalker	2.8238×10^{6}	8.9816×10^{3}
FASTSIM	2.0125×10^{4}	1.6439
Polach	1.9994×10^{4}	73.8518
Heuristic	1.9995×10^{4}	63.5967

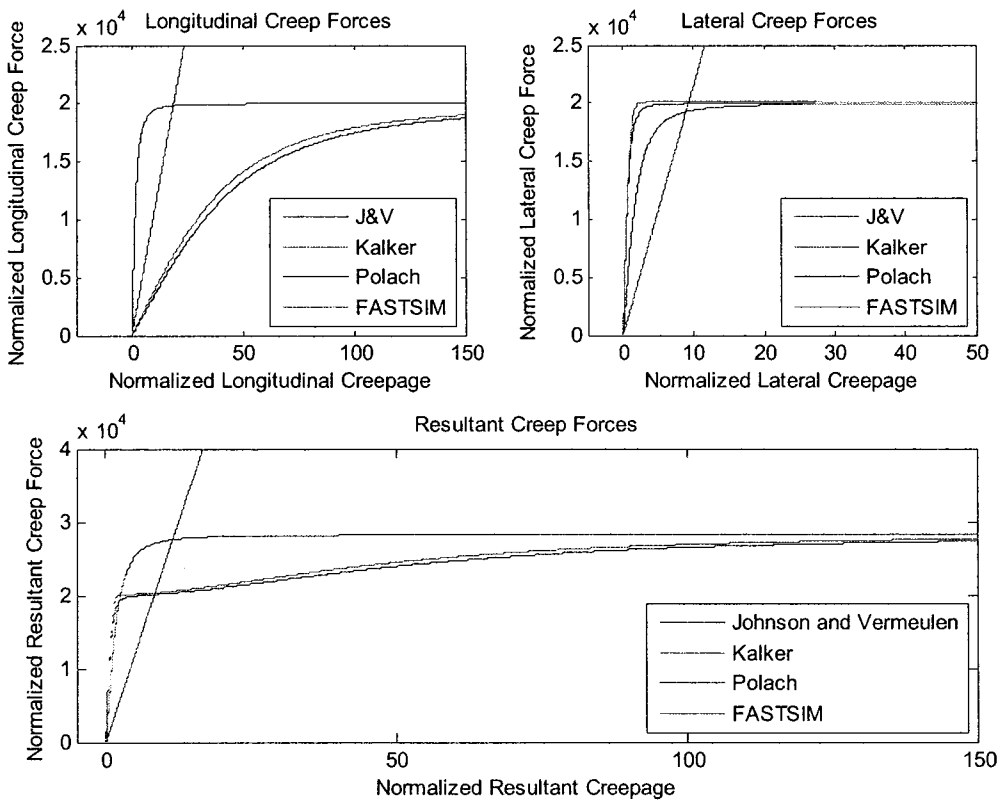

Figure 4.5 – Saturation Law (creep forces are shown in Newtons)

Table 4.2 is then reproduced as a figure with the Kalker theory removed. Figure 4.6 shows that all four theories are very close in F_x. For F_y, it may seem that Heuristic and Polach are close while Johnson and Vermeulen, and FASTSIM are much less. However, considering the very different scales in F_x and F_y, it is concluded that the four theories are very close.

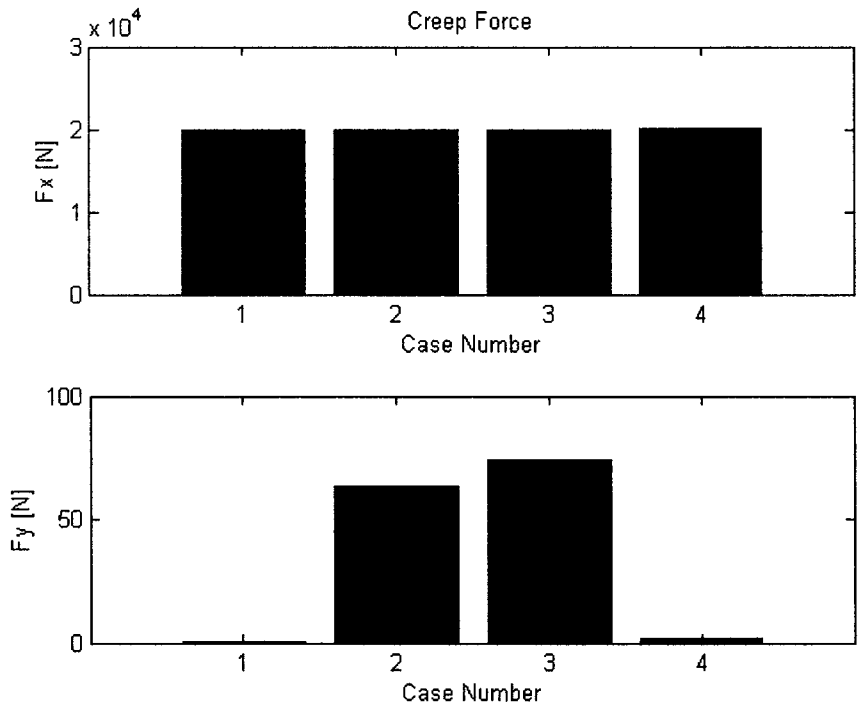

Figure 4.6 – Creep Forces by the Four Theories

(1 - Johnson and Vermeulen, 2 - Heuristic, 3 - Polach, 4 - FASTSIM)

Computation times are depicted in Figure 4.7. The Johnson and Vermeulen theory requires much longer to calculate due to the elliptical integrals used in the calculation. The Kalker, Heuristic, and Polach theories require similar time for calculation. FASTSIM

is included solely for reference, but surprisingly is not as fast as Heuristic or Polach, all being nonlinear.

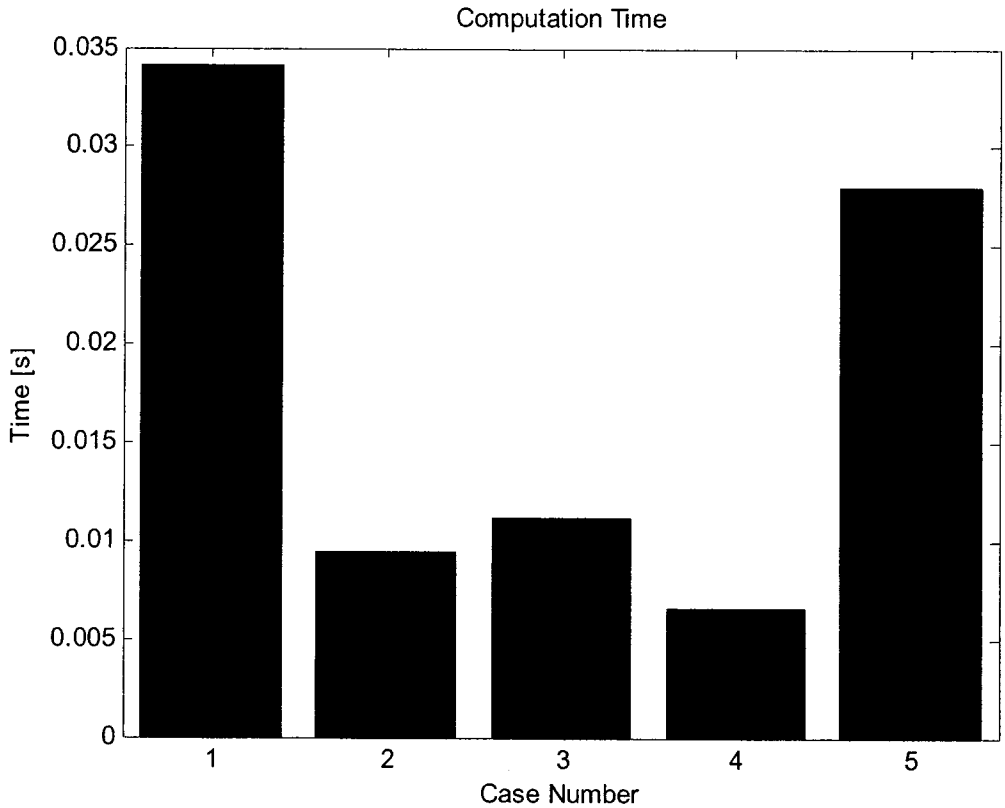

Figure 4.7 – Computation Times by the Five Theories

(1 - Johnson and Vermeulen, 2 - Kalker, 3 - Heuristic, 4 – Polach, 5 – FASTSIM)

4.2 Benchmarking of Track Position-Dependant Creep

4.2.1 Manchester Benchmarks

The Manchester Benchmarks for rail vehicle simulation, established in the late 1990s, was an effort to benchmark existing software packages for rail vehicle simulation for

designers and researchers looking at dynamic vehicle behavior. The Manchester Benchmarks feature a passenger train and a cargo train on several different track cases [4.3]. One of these track cases will be used in this thesis. In this chapter, the track position-dependant creep was tested with the use of Track Case 2 (TC2).

TC2 is described as [4.3] "the track input comprises a 50 m straight section of track followed by a 5 mm lateral shift in the centerline taking place over a distance of 0.1 m in the direction of travel. The gauge remains constant throughout and the track is perfectly level." Figure 4.8 depicts TC2 from the perspective of yaw (rotation about the vertical), pitch (rotation about the lateral), and roll (rotation about the longitudinal) angles relative to the longitudinal distance. Pitch and roll remain zero.

4.2.2 Benchmarking of Track Position-Dependant Creep

The track position-dependant benchmarking is preformed with the forward speed V taken to be constant, hence zero acceleration in the longitudinal direction. Results of the benchmarking can be seen in Figures 4.9 and 4.10.

From Figure 4.9, it is seen that the Heuristic and Polach theories give almost identical results. The Kalker theory leads to a constant F_x whose value is comparable to that of Heuristic or Polach. However, the lateral creep force over the shift by the Kalker theory is twice as large as that by Heuristic or Polach. The results by the Johnson and Vermeulen theory do not bear much resemblance to the other results.

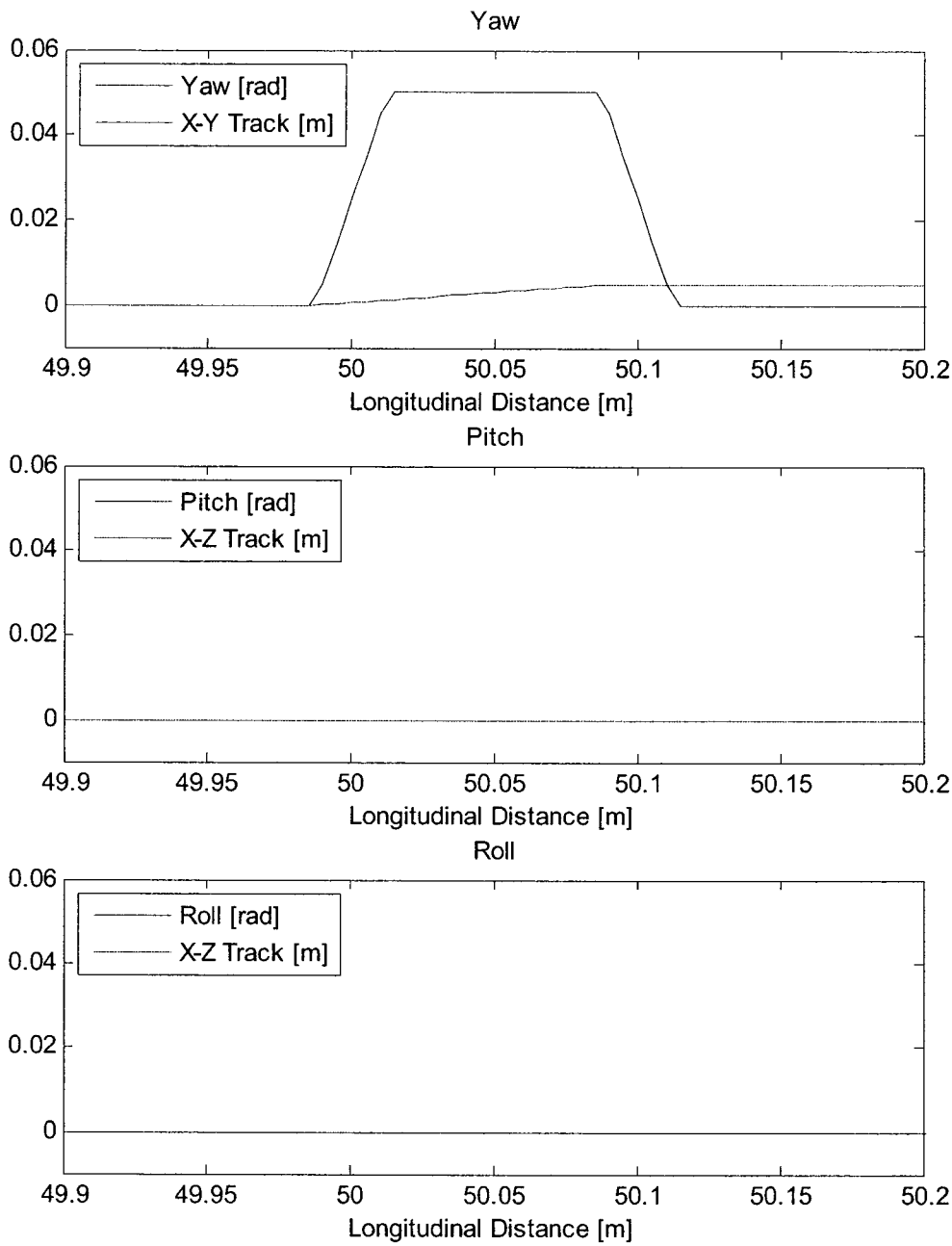

Figure 4.8 – Manchester Benchmarks Track Case 2

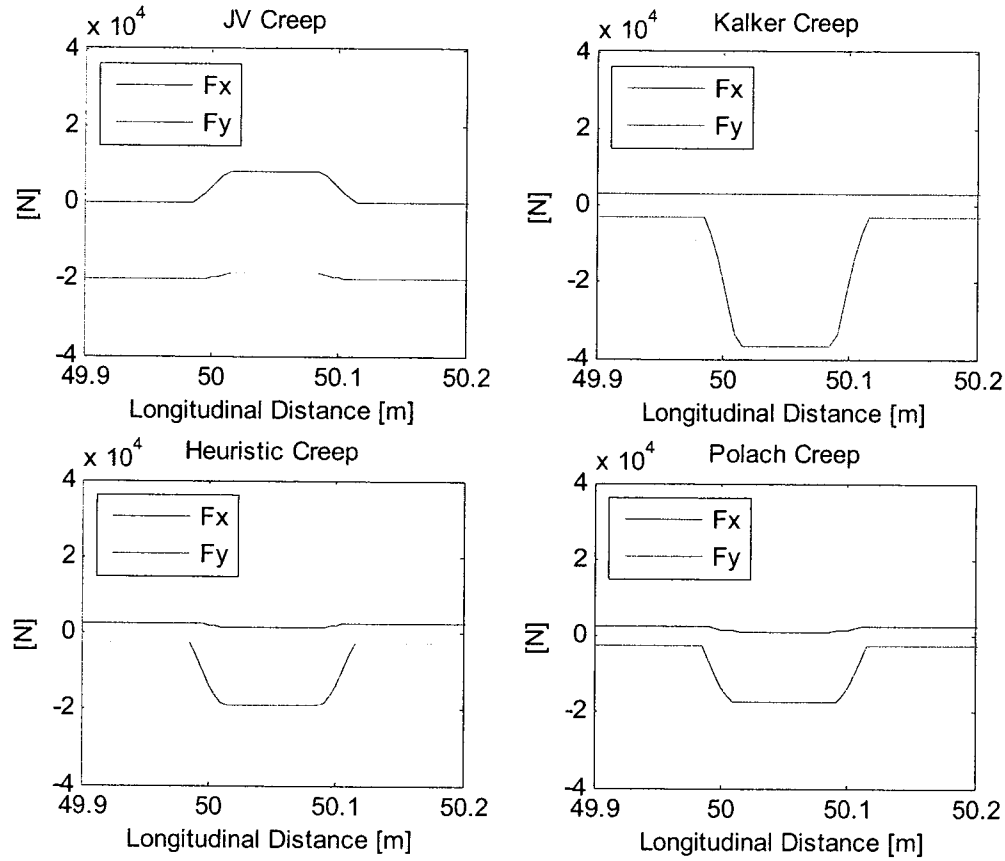

Figure 4.9 – Creep Forces of Track Case 2

Figure 4.10 contrasts the Polach theory with FASTSIM. The creep forces are very close but the computation time by FASTSIM is 30% longer than that of Polach. Overall, with accuracy and computation time considered, the Polach theory will be the preferred choice for the remainder of this thesis.

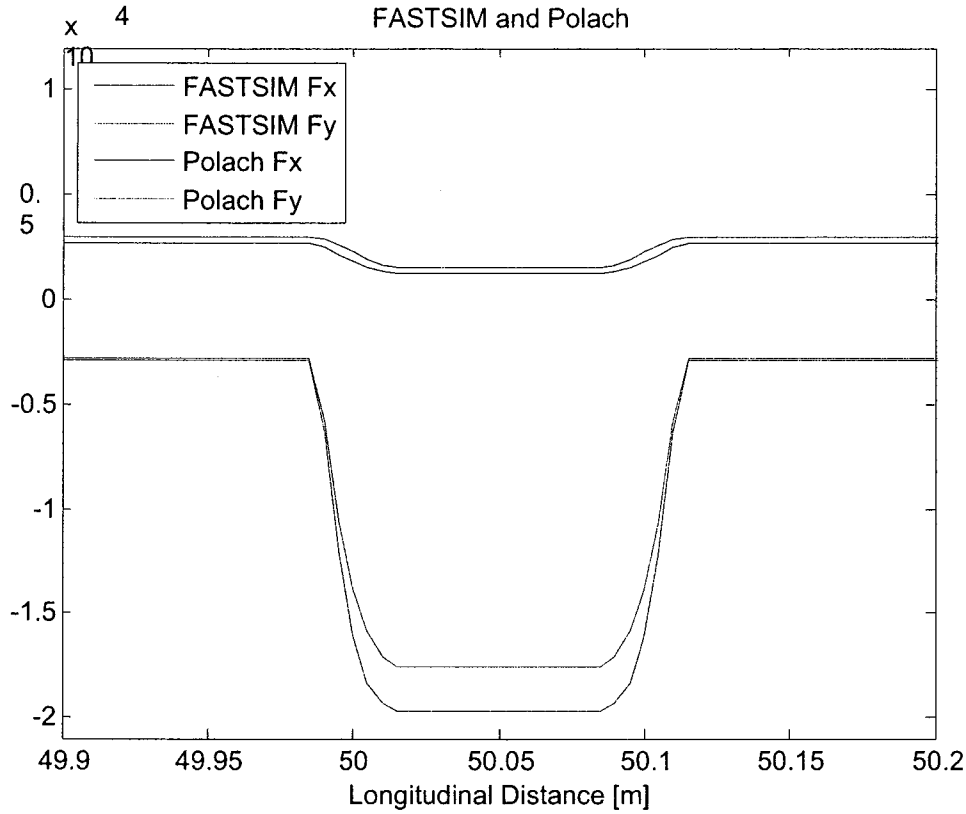

Figure 4.10 – Creep Forces of Track Case 2 with Polach and FASTSIM

(forces are shown in Newtons)

4.3 Dynamic Benchmarking of Creep

For the dynamic benchmarking, three models will be used. Model I is developed on the basis of the model used in *Influence of Yaw Stiffness on the Nonlinear Dynamics of a Railway Wheelset* [4.4], while Model II is taken directly from [4.4]. Model I utilizes dynamic creep forces developed in Chapter 3. It also includes additional penetrations at wheel-rail contact points and the corresponding dynamic normal forces. Model II, on the other hand, utilizes static creep forces which are calculated by the Johnson and

Vermeulen theory. Model III is taken from *Dynamics of Railway Vehicle Systems* [4.5] and uses pre-calculated creep force coefficients.

4.3.1 Model I

Model I is based on that from *Influence of Yaw Stiffness on the Nonlinear Dynamics of a Railway Wheelset* [4.4]. A schematic of the wheelset model is shown in Figure 4.11.

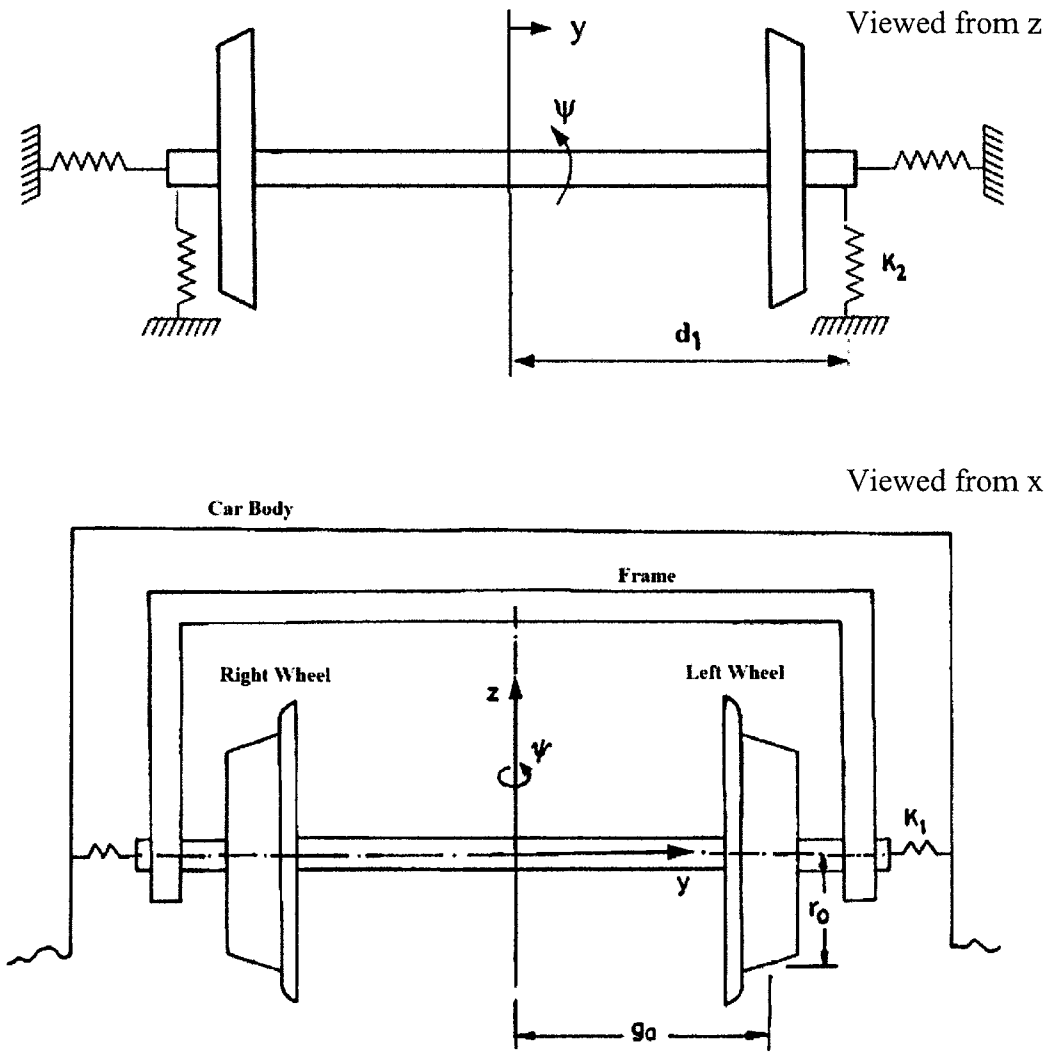

Figure 4.11 – Geometry of Wheelset and Coordinate System

It has two wheels rigidly connected with an axle rolling on a rail that is assumed "knife-edged". The wheels are conical with slope λ and rolling radius r_0. The restoring force from the flanges on the wheels is approximated by a strong linear spring with a dead band and no damping. The lateral motion is restricted by linear springs with no damping. The wheels and the axle are assumed to be rigid bodies. The wheelset is considered to have two degrees of freedom. The first is the lateral displacement y and the second is the yaw motion ψ. The two equations of motion of the wheelset are coupled through the nonlinear creep forces. They are,

$$m_w\ddot{y} + 2k_1 y + 2F_Y(y,\dot{y},\psi,\dot{\psi}) + F_T(y) = 0 \tag{4.1a}$$

$$I_{wz}\ddot{\psi} + 2k_2 d_1^2\psi + g_a F_X(y,\dot{y},\psi,\dot{\psi}) = 0 \tag{4.1b}$$

where m_w is the mass of the wheelset, I_{wz} is the mass moment of inertia of the wheelset about the z-axis, k_1 is the lateral spring constant, k_2 is the yaw spring constant, F_X is the longitudinal creep force, F_Y is the lateral creep force, F_T is the flange force, d_1 is the distance from the centre of gravity to the yaw spring, and g_a is the half-track gauge. In equation (4.1), a single over-dot indicates a first-order time derivative, while a double over-dot denotes a second-order time derivative. F_X and F_Y are functions of $y,\dot{y},\psi,\dot{\psi}$. They need to be updated at every time step. The process of determining F_X and F_Y will be detailed below.

1. First, the static normal force N_0 is determined.

2. The factors K_1, K_2, K_3, and K_4 of equations (3.1-3.4) are calculated, followed by m, n and θ of equations (3.5-3.7). Then, semi-axes a and b are calculated,

$$a = m\left[\frac{3\pi N_0(K_1+K_2)}{4K_3}\right]^{\frac{1}{3}} \tag{4.2}$$

$$b = n\left[\frac{3\pi N_0(K_1+K_2)}{4K_3}\right]^{\frac{1}{3}} \tag{4.3}$$

3. Static penetration is determined by

$$P_0 = -K_3 b^2\left(1+\frac{e^2}{2(1-e^2)}(1-\cos\theta)\right) \tag{4.4}$$

With

$$\begin{aligned} e^2 &= 1-(a/b)^2 \quad \text{for } a<b \\ e^2 &= 1-(b/a)^2 \quad \text{for } a \geq b \end{aligned} \tag{4.5a-b}$$

4. Kalker coefficients c_{11}, c_{22}, c_{23}, and c_{33} of equations (3.28-3.31) are calculated.

5. Next, roll and yaw of the wheelset are updated. Wheelset pitch is not updated as pitch is in the direction of rolling which is not accounted for by the equations of motion (4.1).

$$\phi^w = \frac{2\lambda y}{g_a} \tag{4.6}$$

$$\psi^w = \psi \tag{4.7}$$

6. A^w of equation (3.17) is recalculated with the ϕ^w and ψ^w determined above.

7. The wheelset's global position coordinates and velocity vectors are updated as,

$$R^w = \begin{bmatrix} x \\ y \\ r_0 + \lambda y \end{bmatrix}, \dot{R}^w = \begin{bmatrix} V \\ \dot{y} \\ \lambda \dot{y} \end{bmatrix} \tag{4.8-4.9}$$

where V is the velocity in the x direction. Similarly, the rail's global position coordinates and velocity vectors are,

$$R^r = \begin{bmatrix} 0 \\ 0 \\ 0 \end{bmatrix}, \dot{R}^r = \begin{bmatrix} 0 \\ 0 \\ 0 \end{bmatrix} \tag{4.10-4.11}$$

Values for R^r and $\dot{R}^r$ are zero due to the fixed condition of the rail. The local angular velocities of the wheelset and rail are,

$$\omega^w = \begin{bmatrix} \frac{2\lambda \dot{y}}{g_a} \\ \frac{V}{r_0} \\ \dot{\psi} \end{bmatrix}, \omega^r = \begin{bmatrix} 0 \\ 0 \\ 0 \end{bmatrix} \tag{4.12-4.13}$$

8. Creep force of the right wheel will be calculated for first, followed by the left.

8.1 The local coordinates of the contact points on the wheel and rail are respectively,

$$\bar{U}_p^w = \begin{bmatrix} 0 \\ -\left(\frac{g_a}{2} + y_R\right) \\ -(r_0 - \lambda y_R) \end{bmatrix}, \bar{U}_p^r = \begin{bmatrix} 0 \\ -\frac{g_a}{2} \\ -r_0 \end{bmatrix} \tag{4.14-4.15}$$

where y_R is the lateral displacement of the right wheel. Due to the conical wheel assumption, $y_R = y$.

8.2 The base unit vectors are,

$$\begin{bmatrix} t_1^r \\ t_2^r \\ n^r \end{bmatrix} = A^w A^c \tag{4.16}$$

where A^c is a transformation matrix that takes into account track conditions and contact angles. For TC2 (see description in Section 4.2.1), A^{tc} is

$$A^c = A^{tc} \begin{bmatrix} 1 & 0 & 0 \\ 0 & \cos(\delta_R) & \sin(\delta_R) \\ 0 & -\sin(\delta_R) & \cos(\delta_R) \end{bmatrix} \tag{4.17a}$$

With

$$A^{tc} = \begin{bmatrix} \cos(\alpha) & -\sin(\alpha) & 0 \\ \sin(\alpha) & \cos(\alpha) & 0 \\ 0 & 0 & 1 \end{bmatrix} \tag{4.17b}$$

where α is the slope of the track profile, expressed as a function of longitudinal coordinate x, with respect to the longitudinal coordinate x. That is, $\alpha = \frac{d\eta}{dx}$ with $\eta = \eta(x)$ being the track profile. Angle δ_R is the contact angle for the right wheel, see Figure 4.12.

8.3 Additional penetration and dynamic normal force are given by [4.6],

$$N = N_0 \left(1 + \frac{P_{d3}}{P_0}\right)^{\frac{3}{2}} \tag{4.18}$$

where P_{d3} is the third element of the following vector and represents additional penetration,

$$P_d = \begin{bmatrix} P_{d1} \\ P_{d2} \\ P_{d3} \end{bmatrix} = A^c(\bar{U}_p^r - \bar{U}_p^w) \tag{4.19}$$

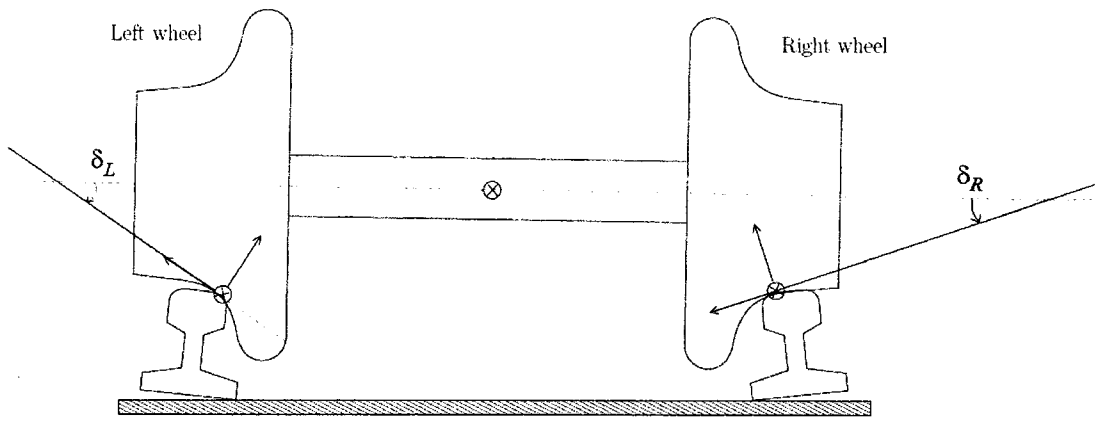

Figure 4.12 – Contact Angles

8.4 The creepages in terms of generalized coordinates and velocities are defined as,

$$\zeta_x = \frac{\left(\dot{r}_p^w - \dot{r}_p^r\right) \cdot t_1^r}{\dot{R}^w t_1^r} \tag{4.20}$$

$$\zeta_y = \frac{\left(\dot{r}_p^w - \dot{r}_p^r\right) \cdot t_2^r}{\dot{R}^w t_1^r} \tag{4.21}$$

$$\varphi = \frac{\left(\omega^w - \omega^r\right) \cdot n^r}{\dot{R}^w t_1^r} \tag{4.22}$$

where $\dot{r}_p^w$ (equation 3.13) and $\dot{r}_p^r$ are the velocity vectors of the wheel and rail contact points respectively. $\dot{r}_p^r$ equals zero due to the fixed nature of the rail.

8.5 Creep forces then need to be calculated. One of the three theories will be used; Kalker (Section 3.4), Heuristic (Section 3.5) or Polach (Section 3.6).

9. Similarly, the left wheel creep forces are calculated as follows. The local coordinates of the contact points on both the wheel and rail are,

$$\bar{U}_p^w = \begin{bmatrix} 0 \\ \frac{g_a}{2} + y_L \\ -(r_0 + \lambda y_L) \end{bmatrix}, \bar{U}_p^r = \begin{bmatrix} 0 \\ \frac{g_a}{2} \\ -r_0 \end{bmatrix} \tag{4.23-4.24}$$

with $y_L = y$. The base unit vectors are,

$$\begin{bmatrix} t_1^r \\ t_2^r \\ n^r \end{bmatrix} = A^w A^c \tag{4.25}$$

Where

$$A_c = \begin{bmatrix} \cos(\alpha) & -\sin(\alpha) & 0 \\ \sin(\alpha) & \cos(\alpha) & 0 \\ 0 & 0 & 1 \end{bmatrix} \begin{bmatrix} 1 & 0 & 0 \\ 0 & \cos(-\delta_L) & \sin(-\delta_L) \\ 0 & -\sin(-\delta_L) & \cos(-\delta_L) \end{bmatrix} \tag{4.26}$$

Here it has been assumed that, magnitude-wise, $\delta_L = \delta_R$, with δ_L being the contact angle on the left wheel (Figure 4.12). Steps 8.3 through 8.5 are then repeated so that the left wheel creep forces are determined.

Finally, the flange contact force in equation (4.1a) is,

$$F_T(y)=\begin{cases} k_r(y-\delta) & y>\delta \\ 0 & -\delta \le y \le \delta \\ k_r(y+\delta) & y<-\delta \end{cases} \tag{4.27}$$

where k_r is the flange spring constant and δ is flange clearance.

4.3.2 Model II

Model II has a similar foundation as Model I, but creep forces are calculated with the Johnson and Vermeulen theory [4.4].

$$m_w\ddot{y}+2k_1y+2F_Y(y,\dot{y},\psi,\dot{\psi})+F_T(y)=0 \tag{4.28a}$$

$$I_{wz}\ddot{\psi}+2k_2d_1^2\psi+g_aF_X(y,\dot{y},\psi,\dot{\psi})=0 \tag{4.28b}$$

where $F_T(y)$ is by equation (4.27). The creep forces F_X and F_Y are given as,

$$F_X=\frac{\zeta_X F_R}{\phi_1\zeta_R},\ F_Y=\frac{\zeta_Y F_R}{\psi_1\zeta_R} \tag{4.29-4.30}$$

with ϕ_1 and ψ_1 being the coefficients defined by equation (3.22). The resulting creep force F_R is,

$$F_R=\mu N_0\begin{cases} \tau-\frac{1}{3}\tau^2+\frac{1}{27}\tau^3 & \tau<3 \\ 1 & \tau\ge 3 \end{cases} \tag{4.31}$$

where

$$\tau = \frac{G\pi ab}{\mu N_0}\zeta_R \tag{4.32}$$

The creepages are,

$$\zeta_X = \frac{\lambda y}{r_0} + \frac{g_a \dot{\psi}}{2V} \tag{4.33}$$

$$\zeta_Y = \frac{\dot{y}}{V} - \psi \tag{4.34}$$

$$\zeta_R = \sqrt{\left(\frac{\zeta_X}{\phi_1}\right)^2 + \left(\frac{\zeta_Y}{\psi_1}\right)^2} \tag{4.35}$$

4.3.3 Model III

Model III is taken from *Dynamics of Railway Vehicle Systems* [4.5]. Model III uses static predetermined creep forces.

$$m_w \ddot{y} + 2k_1 y + \frac{2f_{11}}{V}(\dot{y} + r_0 \frac{2\lambda}{g_a}\dot{y} - V\psi) + F_T(y) = 0 \tag{4.36}$$

$$I_{wz}\ddot{\psi} + 2k_2 d_1^2 \psi + g_a f_{33}\left(\frac{\lambda}{r_0} y + \frac{g_a}{2V}\dot{\psi}\right) = 0 \tag{4.37}$$

where f_{11} is the lateral creep force coefficient, f_{33} is the longitudinal creep force coefficient. A comparison of the key features of the three models is listed in Table 4.3.

Table 4.3 – Model Contrasts

	Model I	Model II	Model III
Creepages	Updated, Large roll and yaw	Updated, Small yaw	Updated, Small roll and yaw
Normal Force	Static or Dynamic	Static	Static
Creep Theory	any	Johnson and Vermeulen, constant values of ϕ_1 and ψ_1	Kalker, constant values of f_{11} and f_{33}
DOF Included	2 (y,ψ)	2 (y,ψ)	2 (y,ψ)

4.3.4 Dynamic Benchmarking

The three models are compared using the parametric values in Table 4.4. Track condition is the Manchester Benchmark's Track Case 2 (see Figure 4.8). This track involves 50 m of straight track followed by a 5 mm lateral shift over 100 mm in the longitudinal direction. The Polach nonlinear theory is used with Model I. The initial condition is a 5 mm lateral displacement, while lateral velocity, yaw, and yaw rate are zero. Forward speed is constant at 8 m/s.

Table 4.4 – Parametric Values for Dynamic Benchmarking

Constant	Value	Description
m_w	1022 *kg*	mass of wheelset
I_{wz}	678 *kg-m*^{2}	moment of inertia
g_a	0.716 *m*	half of the track gauge
λ	0.05	slope of conical wheel
δ	9.1 *mm*	dead band
d_1	0.620 *m*	distance from center of gravity to k_2
k_r	14.60 *MN/m*	spring constant (flange)
k_1	18.23 *kN/m*	spring constant (lateral)
k_2	180 *N/m*	spring constant (yaw)
r_0	0.4572 *m*	centered wheel rolling radius
f_{11}	90.712 *kN*	lateral creep force coefficient
f_{33}	103.228 *kN*	longitudinal creep force coefficient
G	808 *MN/m*^{2}	shear modulus
Ψ_1	0.54192	constant
Φ_1	0.60252	constant
a_e	6.578 *mm*	major semi-axis of contact ellipse
b_e	3.934 *mm*	minor semi-axis of contact ellipse
μ	0.15	coefficient of friction
μN_0*	10 *kN*	adhesive force

* N_0 is the static vertical force between wheel and rail.

Figures 4.13 and 4.14 contrast Models I, II, and III over the TC2 track case. From the plots it can be seen that Models I and II follow a similar but slightly out-of-sync response in lateral displacement, lateral velocity, yaw angle, and yaw rate. Model III yields dynamic responses of a similar frequency, but substantially smaller amplitude. These responses also demonstrate high damping characteristics.

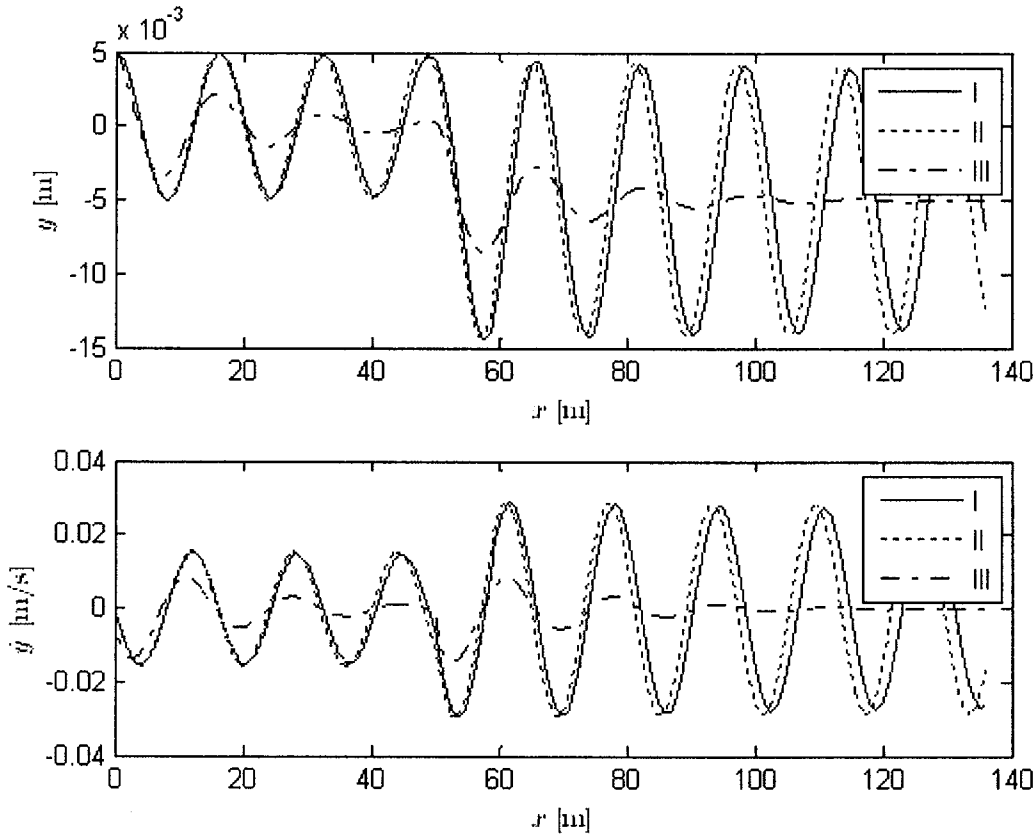

Figure 4.13 – Model Response in the Lateral Direction (TC2)

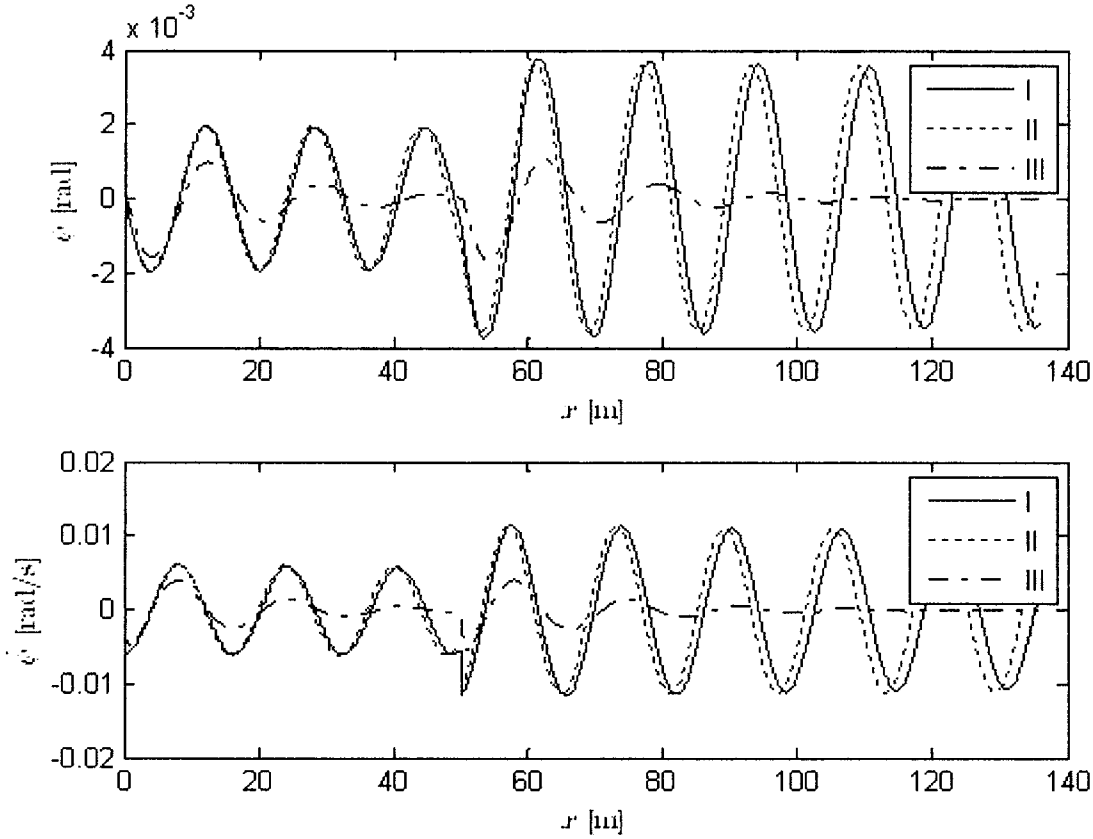

Figure 4.14 – Model Response for the Yaw (TC2)

The following comments can be made.

- The closeness of responses from Models I and II verifies the 9-step process of determining dynamic creep forces and moment as given in Section 4.3.1.
- Polach theory, which is used with Model I due to its accuracy and computational efficiency, enables the model to satisfactorily capture and represent the dynamic responses of the wheelset.
- The different response characteristics from Model III are due to the use of Kalker theory which typically predicts much higher values of creep forces, leading to smaller responses.

- Model II is limited to small roll and yaw. Conversely, Model I is not subject to such restriction. As will be seen in Chapter 5, Model I will be used with realistic wheel and rail profiles which can lead to large roll and yaw responses.

4.4 Concluding Remarks

Benchmarking conducted in this chapter shows that the Polach nonlinear theory of creep is accurate and computationally efficient. This theory will be used in the next chapter for the investigation of wheelset responses where realistic wheel and rail profiles are considered. This chapter also verified the nine-step process of updating dynamic creep forces and moment. This process will also be utilized in Chapter 5.

Chapter 5 – Dynamic Responses of a Single-Axle Wheelset Incorporating Profiled Wheels and Rails

Chapter 4 has shown that Model I, together with the Polach theory, is capable of satisfactorily capturing and representing the dynamic behaviour of a single-axle wheelset and is computationally efficient. However, Model I was based on the assumption of conical wheels and knife-edged rails. Such assumptions are not realistic. Therefore, realistic or profiled wheels and rails will be investigated in this chapter.

5.1 Wheel and Rail Profiles

The profiled wheel examined in this thesis is the AAR (Association of American Railroads) 1:20 wheel as shown in Figure 5.1. This wheel profiles a 7° tread angle, followed by a 70° flange, followed by a 58° flange tread. The rail profile is depicted in Figure 5.2.

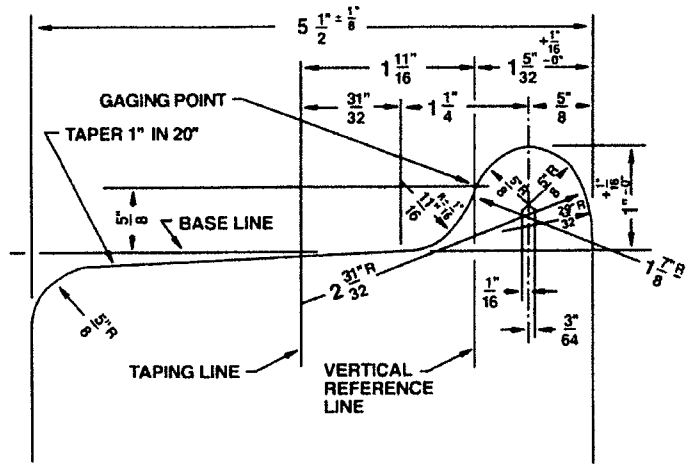

Figure 5.1 –Wheel Profile [5.1]

Under normal conditions, the wheels will operate on the 7° treads, where there is only one point of contact per wheel-rail combination. Larger lateral movements will cause a two-point contact, at the tread and the flange, between the right wheel and rail, for example, while the left wheel and rail remain in one-point tread contact condition. Larger lateral movements still can cause the wheel to ride on the top of the flange. Although this is a one-point contact, it creates a large roll angle and a large left and right wheel radii inequality. Physically, it represents a dangerous situation to the rail vehicle.

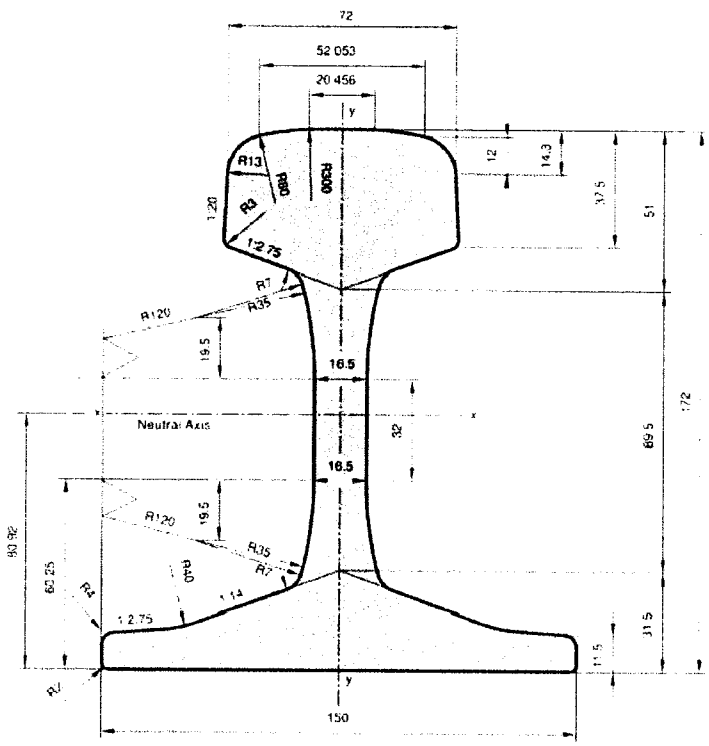

Figure 5.2 – Rail Profile [5.1]

With the use of a profiled wheel and rail, the dependence of rolling radius R_L^w or R_R^w, and contact angle δ_R or δ_L, on lateral displacement y becomes complex and is usually pre-determined. Figure 5.3 and 5.4 show rolling radius of wheel (left or right) and contact angle of wheel (again left or right) as functions of lateral displacement y [5.2].

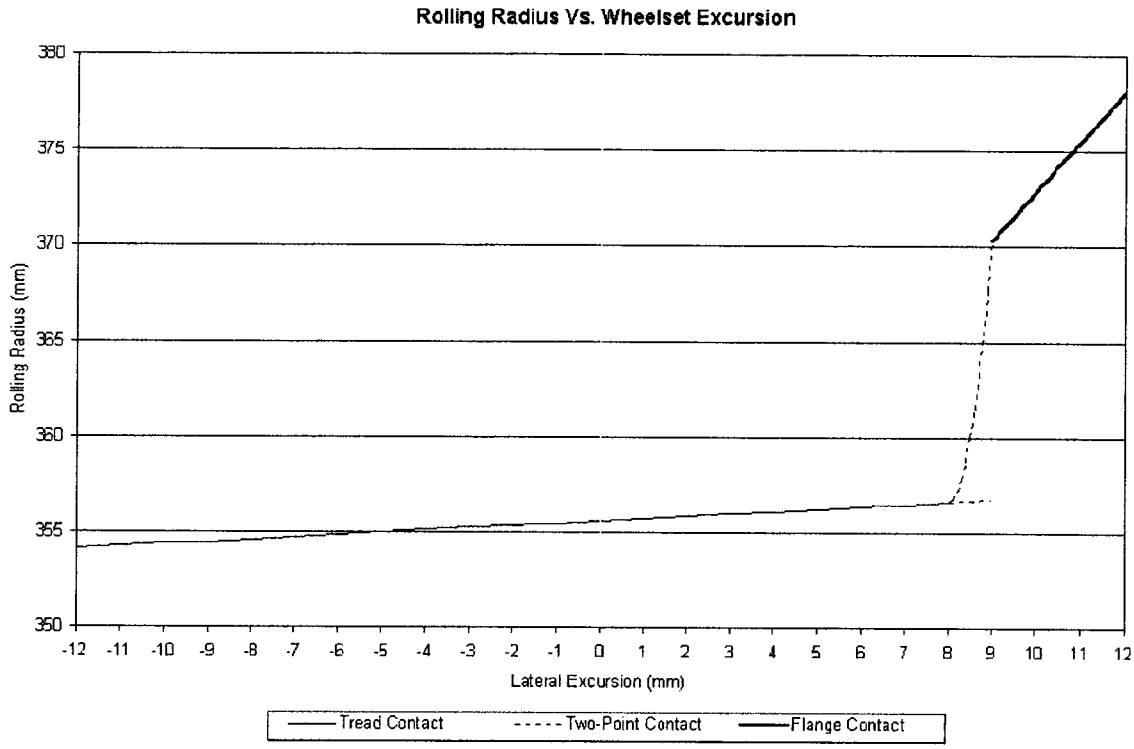

Figure 5.3 – Rolling Radius versus Lateral Displacement [5.2]

The following define the radii; r_{tl} the left tread, r_{fl} the left flange, r_{tr} the right tread, and r_{fr} the right flange. These radii form the plot in Figure 5.3.

$$r_{tl} = r_0 + 0.125y \qquad |y| \le 0.008 \tag{5.1}$$

$$r_{fl} = \begin{cases} 0.3566 + 13700(y - 0.008)^2 & 0.008 \ge y > 0.009 \\ 0.3703 + 2.5833(y - 0.009) & y \ge 0.009 \end{cases} \tag{5.2}$$

$$r_{tr} = r_0 - 0.125y \tag{5.3}$$

$$r_{fr} = \begin{cases} 0.3703 + 2.5833(-y - 0.009) & y \le -0.009 \\ 0.3566 + 13700(-y - 0.008)^2 & -0.009 > y \ge -0.008 \end{cases} \tag{5.4}$$

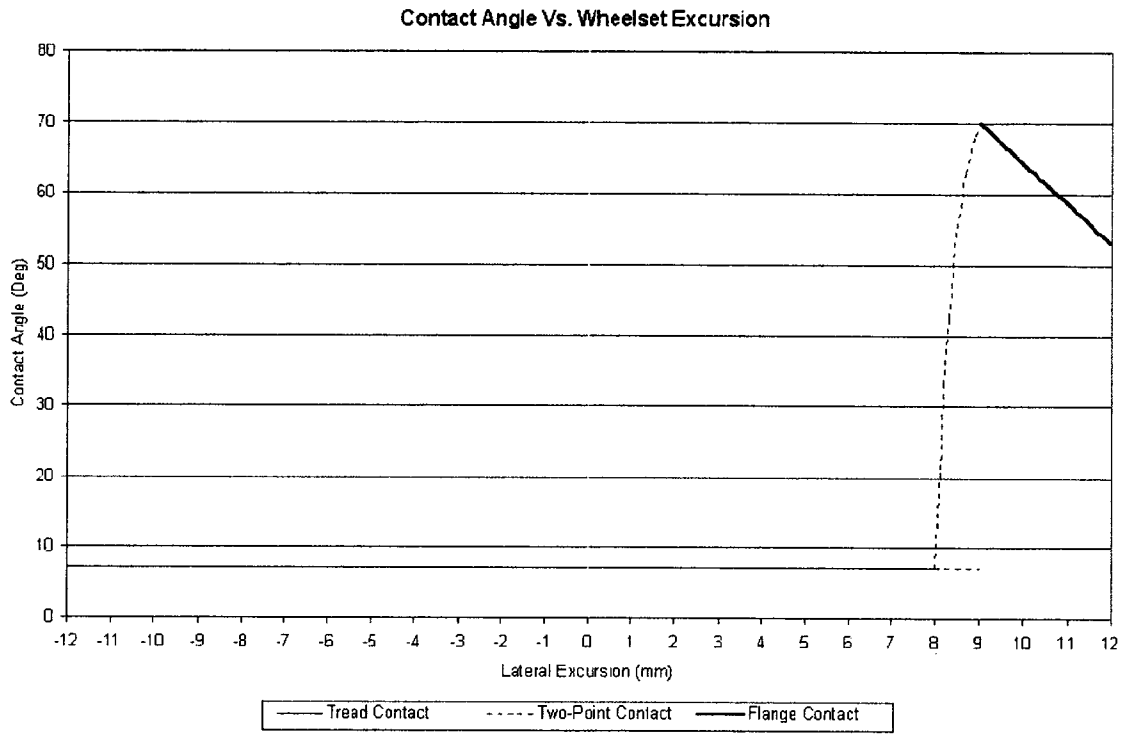

Figure 5.4 – Contact Angle versus Lateral Displacement [5.2]

The following define the contact angles; c_{tl} the left tread, c_{fl} the left flange, c_{tr} the right tread, and c_{fr} the right flange. These contact angles form the plot in Figure 5.4.

$$c_{tl} = \tan^{-1}(0.125) \qquad |y| \le 0.008 \tag{5.5}$$

$$c_{fl} = \begin{cases} \tan^{-1}\left[0.125 + 2648(y - 0.008)\right] & 0.008 \ge y > 0.009 \\ \tan^{-1}(2.748) & y \ge 0.009 \end{cases} \tag{5.6}$$

$$c_{tr} = \tan^{-1}(0.125) \tag{5.7}$$

$$c_{fr} = \begin{cases} \tan^{-1}(2.748) & y \le -0.009 \\ \tan^{-1}\left[0.125 + 2648(-y - 0.008)\right] & -0.009 > y \ge -0.008 \end{cases} \tag{5.8}$$

In the next two sections, a new wheelset dynamic model will be introduced. This model (for easily reference, will be called the Modified-Garg model) is more realistic. It calculates for normal forces at every time step and can accept both small and large angles. It uses track-dependant creep forces (Section 4.2.2), and profiled wheels and rail. Contact conditions include both one-point at tread and at flange, and two-point.

5.2 Single Point Contact

Single point contact occurs in two situations. The first, the normal operating condition, is when both wheels are running on the 7° wheel treads. This corresponds to the conical wheel condition, if the wheels are not worn. The second is when one wheel is running on top of the flange while the opposite wheel is on the wheel tread. Mathematically, the two situations can be treated the same. In the following sub-sections, the point of contact is not identified, as it can be a tread contact point or a flange contact point.

5.2.1 Degrees of Freedom

A rigid body has six degrees of freedom; displacements *x, y, z*, and rotations roll, pitch and yaw, see Figure 5.5. With reference to the free body diagram in Figure 5.6, the six corresponding governing equations of motion are [5.3],

Longitudinal Equation:

$$m_w \ddot{x} = F_{Lx} + F_{Rx} + N_{Rx} + N_{Lx} + F_{sx} \tag{5.9}$$

Lateral Equation:

$$m_w \ddot{y} = F_{Ly} + F_{Ry} + N_{Ry} + N_{Ly} + F_{sy} \tag{5.10}$$

Vertical Equation:

$$m_w \ddot{z} = F_{Lz} + F_{Rz} + N_{Rz} + N_{Lz} + F_{sz} - W_a \tag{5.11}$$

Roll Equation:

$$\begin{aligned} I_{wx}\ddot{\phi} = I_{wy}\left(\frac{V}{r_0}\right)\dot{\psi} + R_{Ry}(F_{Rz} + N_{Rz}) - R_{Rz}(F_{Ry} + N_{Ry}) \\ + R_{Ly}(F_{Lz} + N_{Lz}) - R_{Lz}(F_{Ly} + N_{Ly}) + M_{Lx} + M_{Rx} + M_{sx} \end{aligned} \tag{5.12}$$

Pitch Equation:

$$\begin{aligned} I_{wy}\ddot{\beta} = R_{Rz}F_{Rx} - R_{Rx}(F_{Rz} + N_{Rz}) + R_{Lz}F_{Lx} \\ - F_{Lx}(F_{Lz} + N_{Lz}) + M_{Ly} + M_{Ry} + M_{sy} \end{aligned} \tag{5.13}$$

Yaw Equation:

$$\begin{aligned} I_{wx}\ddot{\psi} = -I_{wy}\left(\frac{V}{r_0}\right)\dot{\phi} + R_{Rx}(F_{Ry} + N_{Ry}) - R_{Ry}F_{Rx} \\ + R_{Lx}(F_{Ly} + N_{Ly}) - R_{Ly}F_{Lx} + M_{Lz} + M_{Rz} + M_{sz} \end{aligned} \tag{5.14}$$

where N means a normal force, F means a creep force, M means a creep moment, and F_s and M_s denotes suspension forces and moments. For N, F and M, the first subscript indicates L(eft) or R(ight) contact point; the second subscript indicates components in the x, y and z directions. The subscript (x or y or z) associated with F_s and M_s denotes the direction of the force and moment component. Finally, R is the position vector draw from the centre of gravity of the wheelset to a contact point. The subscripts of R follow the

convention used with N or F or M. It should be mentioned that the spin β in equation (5.13) is defined as the deviation of the time-dependent pitch over the nominal pitch V/r_0. Symbols m_w, I_{wx}, I_{wy} and I_{wz} denote the mass of wheelset, and the mass moments of inertia of the wheelset about the x, y and z axes, respectively. Lastly, W_a is the pay load on the wheelset.

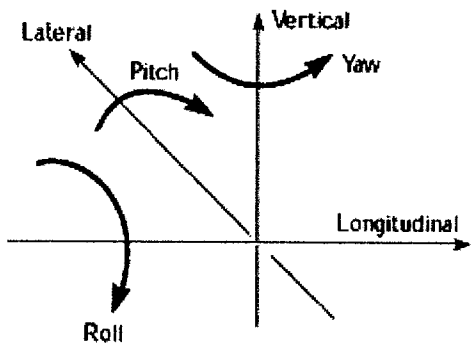

Figure 5.5 – Six Degrees of Freedom

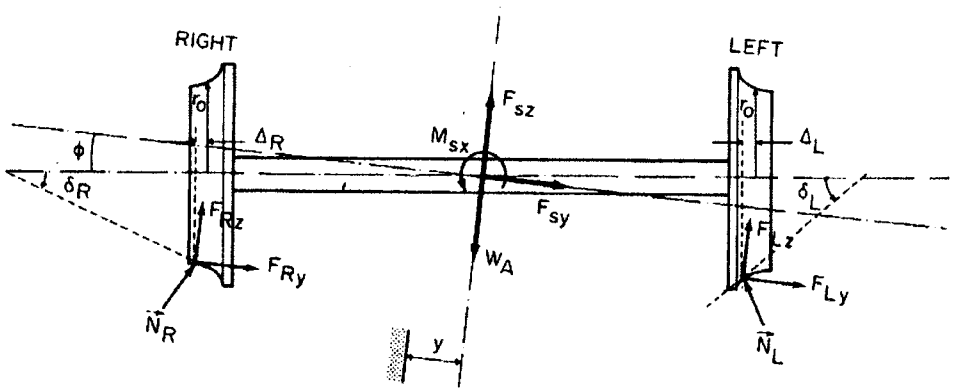

Figure 5.6 – Free Body Diagram of the Wheelset [5.3]

Since this thesis focuses on only the lateral dynamics and with the use of constant forward velocity V, the degrees of freedom in the x and pitch directions need not be considered. As a result, the pair of equations (5.9) and (5.13) are omitted. In addition, due

to the geometrical constraints imposed by the contact of wheel to rail, the degrees of freedom in the z and roll directions are now dependant on the lateral movement of the wheelset. However, equations (5.11) and (5.12) can not be simply omitted. Instead they will be used to determine normal forces developed in the contact points, as will be shown the sub-section below.

5.2.2 Normal Forces – Single Point Contact

As mentioned earlier, equations (5.11) and (5.12) will be used to determine the normal forces. Equation (5.11) is rewritten as,

$$\begin{aligned} N_{Lz} + N_{Rz} &= m\ddot{z} + W_a - F_{Lz} - F_{Rz} - F_{sz} \\ &= F_d \end{aligned} \tag{5.15}$$

with the right-hand side denoted as F_d for simplicity. Similarly from (5.12),

$$\begin{aligned} R_{Ly}N_{Lz} + R_{Ry}N_{Rz} - R_{Lz}N_{Ly} - R_{Rz}N_{Ry} &= I_{wx}\ddot{\phi} - I_{wy}\left(\frac{V}{r_0}\right)\dot{\psi} - R_{Ly}F_{Lz} + R_{Lz}F_{Ly} - M_{Lx} - M_{Rx} \\ &\quad - M_{sx} - R_{Ry}F_{Rz} + R_{Rz}F_{Ry} \\ &= M_d \end{aligned} \tag{5.16}$$

Since

$$\mathbf{N_R} = N_R\mathbf{n_r}\,,\ \mathbf{N_L} = N_L\mathbf{n_l} \tag{5.17-5.18}$$

or

$$\begin{Bmatrix} N_{Rx} \\ N_{Ry} \\ N_{Rz} \end{Bmatrix} = N_R \begin{Bmatrix} n_x^r \\ n_y^r \\ n_z^r \end{Bmatrix}\,,\quad \begin{Bmatrix} N_{Lx} \\ N_{Ly} \\ N_{Lz} \end{Bmatrix} = N_L \begin{Bmatrix} n_x^l \\ n_y^l \\ n_z^l \end{Bmatrix} \tag{5.19-5.20}$$

Equations (5.15) and (5.16) become, in matrix form

$$\begin{bmatrix} n_z^l & n_z^r \\ R_{Ly}n_z^l - R_{Lz}n_y^l & R_{Ry}n_z^r - R_{Lz}n_y^r \end{bmatrix} \begin{Bmatrix} N_L \\ N_R \end{Bmatrix} = \begin{Bmatrix} F_d \\ M_d \end{Bmatrix} \tag{5.21}$$

By using respective velocity and acceleration values at the previous step (which are known), instead of the unknown values at the current step, N_L and N_R can be solved from equation (5.21).

These normal forces are then used to determine creep forces and moment (see the 9-step process in Section 4.3.1 with $N_0 = N_L$ or $N_0 = N_R$). Meanwhile, the lateral components of these forces are evaluated by

$$N_{Ly} = N_L n_y^l \tag{5.22}$$

$$N_{Ry} = N_R n_y^r \tag{5.23}$$

Such forces and moment are to be used in the equations of motion.

5.2.3 Equations of Motion – Single Point Contact

The equations of motion used to describe single point contact are as follows:

$$m_w \ddot{y} = F_{Ly} + F_{Ry} + N_{Ry} + N_{Ly} + F_{sy} \tag{5.24}$$

$$\begin{aligned} I_{wx}\ddot{\psi} = &-I_{wy}\left(\frac{V}{r_0}\right)\dot{\phi} + R_{Rx}(F_{Ry} + N_{Ry}) - R_{Ry}F_{Rx} \\ &+ R_{Lx}(F_{Ly} + N_{Ly}) - R_{Ly}F_{Lx} + M_{Lz} + M_{Rz} + M_{sz} \end{aligned} \tag{5.25}$$

Once equations (5.24) and (5.25) are solved, vertical displacement, velocity and acceleration, and roll angle, velocity and acceleration are determined, on the basis of dependence of such terms on the lateral displacement, velocity and acceleration. That is, for single point contact, if r_r and r_l are the rolling radii:

$$r_r = \begin{cases} r_{tr} & y > -0.008 \\ \text{or} & \\ r_{fr} & y \le -0.009 \end{cases}, \quad r_l = \begin{cases} r_{tl} & y < 0.008 \\ \text{or} & \\ r_{fl} & y \ge 0.009 \end{cases} \tag{5.26a-5.26b}$$

Vertical displacement at the centre of gravity, z, is then given as:

$$z = \frac{1}{2}(r_l + r_r) - r_0 \tag{5.27}$$

Vertical velocity and acceleration are:

$$\dot{z} = \frac{\dot{y}}{2}\left[\frac{dr_l(y)}{dy} + \frac{dr_r(y)}{dy}\right] \tag{5.28}$$

$$\ddot{z} = \frac{\ddot{y}}{2}\left[\frac{dr_l(y)}{dy} + \frac{dr_r(y)}{dy}\right] + \frac{\dot{y}^2}{2}\left[\frac{d^2r_l(y)}{dy^2} + \frac{d^2r_r(y)}{dy^2}\right] \tag{5.29}$$

The roll angle of the wheelset is given as:

$$\phi = \frac{r_l(y) - r_r(y)}{2g_a} \tag{5.30}$$

Lastly, roll velocity and acceleration are given as:

$$\dot{\phi} = \frac{\dot{y}}{2g_a}\left[\frac{dr_l(y)}{dy} - \frac{dr_r(y)}{dy}\right] \tag{5.31}$$

$$\ddot{\phi} = \frac{\ddot{y}}{2g_a}\left[\frac{dr_l(y)}{dy} - \frac{dr_r(y)}{dy}\right] + \frac{\dot{y}^2}{2g_a}\left[\frac{d^2r_l(y)}{dy^2} - \frac{d^2r_r(y)}{dy^2}\right] \tag{5.32}$$

5.3 Two-Point Contact

In the following, it is assumed that the two-point contact occurs between the right wheel and rail. The case of two-point contact between the left wheel and rail can be derived in a similar manner. The six equations of motion governing longitudinal, lateral, vertical, roll, pitch, and yaw are now,

Longitudinal Equation:

$$m\ddot{x} = F_{Lx} + F_{Rx} + F_{Rxf} + N_{Rx} + N_{Rxf} + N_{Lx} + F_{sx} \tag{5.33}$$

Lateral Equation:

$$m\ddot{y} = F_{Ly} + F_{Ry} + F_{Ryf} + N_{Ry} + N_{Ryf} + N_{Ly} + F_{sy} \tag{5.34}$$

Vertical Equation:

$$m\ddot{z} = F_{Lz} + F_{Rz} + F_{Rzf} + N_{Rz} + N_{Rzf} + N_{Lz} + F_{sz} - W_a \tag{5.35}$$

Roll Equation:

$$\begin{aligned} I_{wx}\ddot{\phi} = I_{wy}\left(\frac{V}{r_0}\right)\dot{\psi} + R_{Ry}(F_{Rz} + N_{Rz}) + R_{Ryf}(F_{Rzf} + N_{Rzf}) \\ - R_{Rz}(F_{Ry} + N_{Ry}) - R_{Rzf}(F_{Ryf} + N_{Ryf}) \\ + R_{Ly}(F_{Lz} + N_{Lz}) - R_{Lz}(F_{Ly} + N_{Ly}) + M_{Lx} + M_{Rx} + M_{Rxf} + M_{sx} \end{aligned} \tag{5.36}$$

Pitch Equation:

$$\begin{aligned} I_{wy}\ddot{\beta} = R_{Rz}F_{Rx} + R_{Rzf}F_{Rxf} - R_{Rx}(F_{Rz} + N_{Rz}) - R_{Rxf}(F_{Rzf} + N_{Rzf}) \\ + R_{Lz}F_{Lx} - F_{Lx}(F_{Lz} + N_{Lz}) + M_{Ly} + M_{Ry} + M_{Ryf} + M_{sy} \end{aligned} \tag{5.37}$$

Yaw Equation:

$$\begin{aligned} I_{wx}\ddot{\psi} = -I_{wy}\left(\frac{V}{r_0}\right)\dot{\phi} + R_{Rx}(F_{Ry} + N_{Ry}) + R_{Rxf}(F_{Ryf} + N_{Ryf}) - R_{Ry}F_{Rx} \\ - R_{Ryf}F_{Rxf} + R_{Lx}(F_{Ly} + N_{Ly}) - R_{Ly}F_{Lx} + M_{Lz} + M_{Rz} + M_{Rzf} + M_{sz} \end{aligned} \tag{5.38}$$

where N_{Ri}, F_{Ri}, R_{Ri} and $M_{Ri}\,(i=x,y,z)$ denote the right side tread normal force, creep force, position vector of contact point to wheelset centre, and creep moment, respectively. As well, N_{Rif}, F_{Rif}, R_{Rif} and $M_{Rif}\,(i=x,y,z)$ denote the right side flange contact normal force, creep force, position vector of contact point to wheelset centre, and creep moment, respectively. Other symbols have the same meanings as in single point contact; see the paragraph following equation (5.14).

5.3.1 Normal Forces – Two-Point Contact

Rewriting (5.34) – (5.36)

$$\begin{aligned} N_{Rzf}+N_{Rz}+N_{Lz} &= m\ddot{z}+W_a-F_{Lz}-F_{Rz}-F_{Rzf}-F_{Sz} \\ &= F_{d1} \end{aligned} \tag{5.39}$$

$$\begin{aligned} N_{Ryf}+N_{Ry}+N_{Ly} &= m\ddot{y}-F_{Ly}-F_{Ry}-F_{Ryf}-F_{Sy} \\ &= F_{d2} \end{aligned} \tag{5.40}$$

$$\begin{aligned} R_{Ryf}N_{RZf}+R_{Ry}N_{Rz}-R_{Rzf}N_{Ryf} & \\ -R_{Rz}N_{Ry}+R_{Ly}N_{Lz}-R_{Lz}N_{Ly} &= I_{wx}\ddot{\phi}-I_{wv}\left(\frac{V}{r_0}\right)\dot{\psi}-R_{Ryf}F_{Rzf}-R_{Ry}F_{Rz}+R_{Rzf}F_{Ryf} \\ &\quad +R_{Rz}F_{Ry}-R_{Ly}F_{Lz}+R_{Lz}F_{Ly}-M_{Lx}-M_{Rx}-M_{Rxf}-M_{Sx} \\ &= M_d \end{aligned} \tag{5.41}$$

Since,

$$\begin{aligned} \mathbf{N}_R &= N_R\mathbf{n}_r & \mathbf{N}_{Rf} &= N_{Rf}\mathbf{n}_{rf} & \mathbf{N}_L &= N_L\mathbf{n}_l \\ &= N_R\begin{Bmatrix} n_x^r \\ n_y^r \\ n_z^r \end{Bmatrix}, & &= N_{Rf}\begin{Bmatrix} n_{xf}^r \\ n_{yf}^r \\ n_{zf}^r \end{Bmatrix}, & &= N_L\begin{Bmatrix} n_x^l \\ n_y^l \\ n_z^l \end{Bmatrix} \end{aligned} \tag{5.42-5.44}$$

Equations (5.39)-(5.41) become,

$$\begin{bmatrix} n_{zf}^r & n_z^r & n_z^l \\ n_{yf}^r & n_y^r & n_y^l \\ \left(R_{Ryf}n_{zf}^r - R_{Rzf}n_{yf}^r\right) & \left(R_{Ry}n_z^r - R_{Rz}n_y^r\right) & \left(R_{Ly}n_z^l - R_{Lz}n_y^l\right) \end{bmatrix} \begin{Bmatrix} N_{Rf} \\ N_R \\ N_L \end{Bmatrix} = \begin{Bmatrix} F_{d1} \\ F_{d2} \\ M_d \end{Bmatrix} \tag{5.45}$$

Again, the respective velocity and accelerations values at the previous time step are used to evaluate the right-hand side of (5.45) so that N_L, N_R and N_{Rf} can be readily solved.

Lastly, the lateral components of such forces are,

$$N_{Ly} = N_L n_y^l \tag{5.46}$$

$$N_{Ry} = N_R n_y^r \tag{5.47}$$

$$N_{Ryf} = N_{Rf} n_{yf}^r \tag{5.48}$$

5.3.2 Equations of Motion – Two Point Contact

The model used to describe right-side two point contact is as follows:

$$m\ddot{y} = F_{Ly} + F_{Ry} + F_{Ryf} + N_{Ly} + N_{Ry} + N_{Ryf} + F_{sy} \tag{5.49}$$

$$\begin{aligned} I_{wx}\ddot{\psi} = &-I_{wy}\left(\frac{V}{r_0}\right)\dot{\phi} + M_{Lz} + M_{Rz} + M_{Rzf} + M_{sz} \\ &+ R_{Rx}(F_{Ry} + N_{Ry}) - R_{Ry}F_{Rx} \\ &+ R_{Rxf}(F_{Ryf} + N_{Ryf}) - R_{Ryf}F_{Rxf} \\ &+ R_{Lx}(F_{Ly} + N_{Ly}) - R_{Ly}F_{Lx} \end{aligned} \tag{5.50}$$

For such a two point contact, the rolling radii are r_r and r_l.

$$r_r = \begin{cases} r_{tr} & y > -0.008 \\ r_{fr} & -0.009 \le y \le -0.008 \end{cases}, \quad r_l = r_{tl} \quad y < 0.008 \qquad (5.51a\text{-}5.51b)$$

with vertical displacement, velocity and acceleration, as well as roll angle, rate and acceleration given by (5.27) – (5.32).

5.4 Case Studies

5.4.1 Response I

Response I is calculated on TC2 (Section 4.2.1) with the same initial disturbance of 5 mm as Section 4.3.4. Initial lateral velocity, yaw angle and yaw rate are all set to zero. Forward velocity is $V = 8$ m/s. Figures 5.7 through 5.10 plot the movement of the wheelset in the lateral, yaw, vertical, and roll directions. The lateral and yaw responses are solved from equations (5.24)-(5 .25), since the initial disturbance and TC2 will only cause single point contact. The vertical and roll plots are calculated as per equations (5.27)-(5.32).

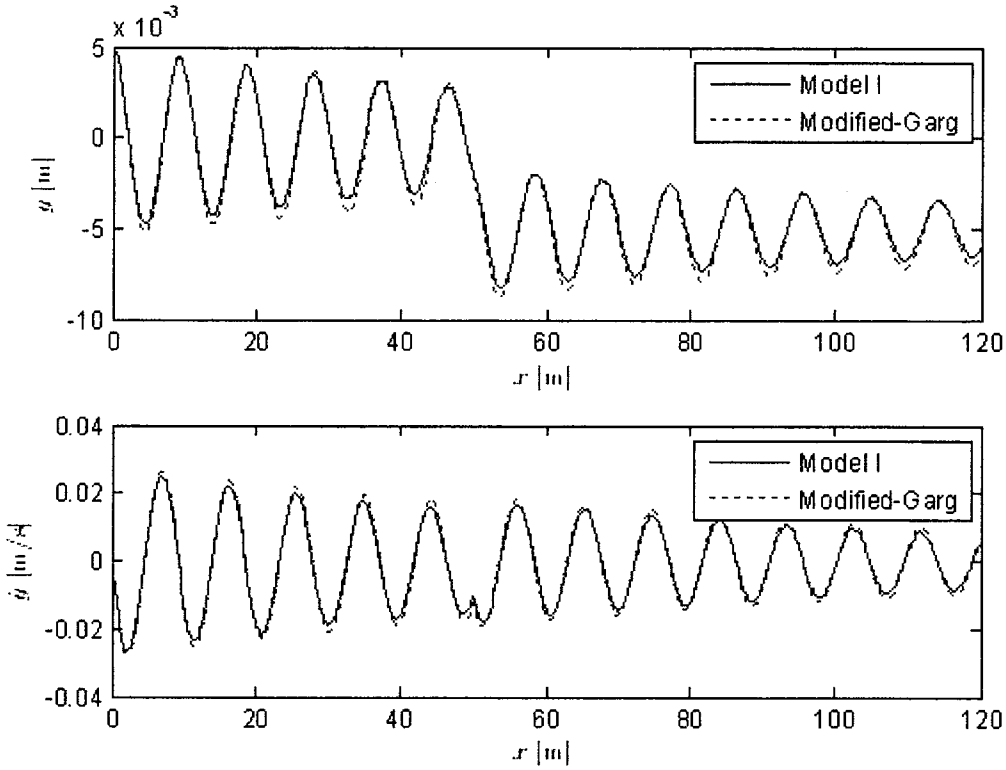

Figure 5.7 – Response I, Lateral Displacement and Velocity

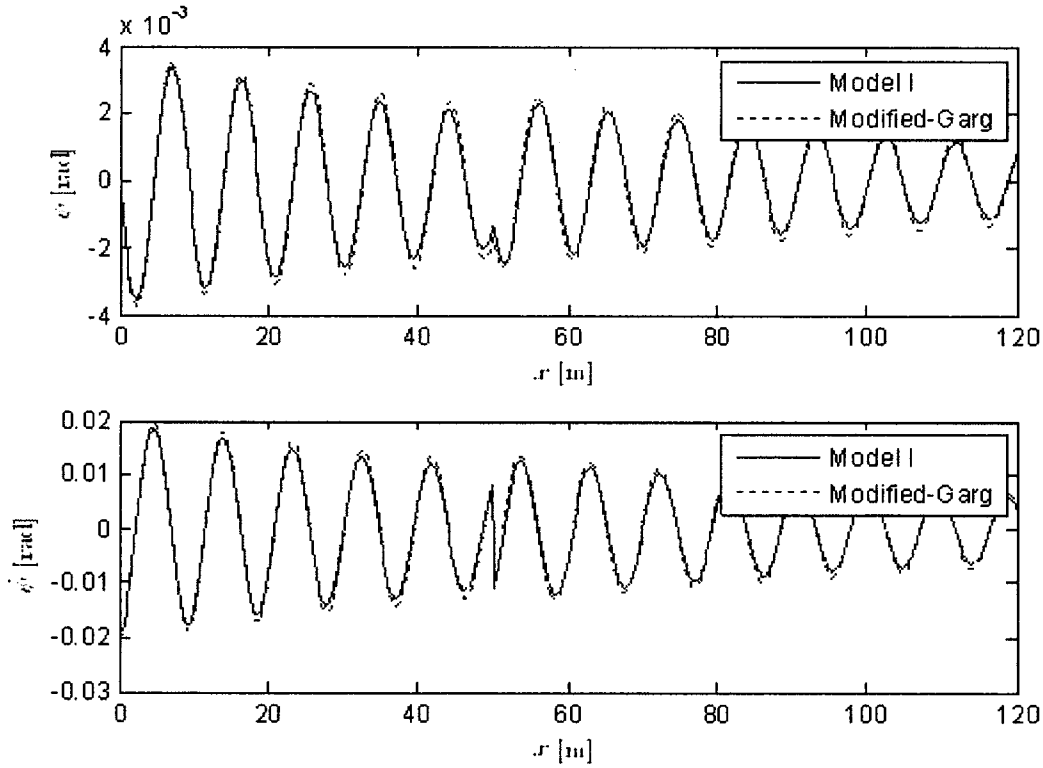

Figure 5.8 – Response I, Yaw Angle and Rate

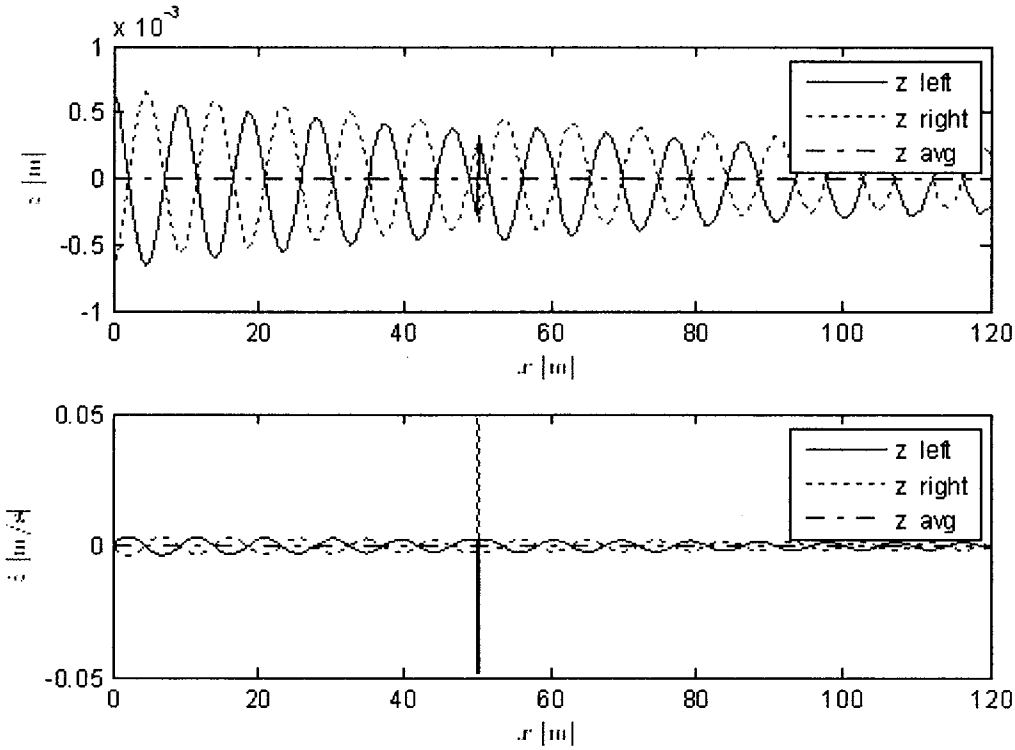

Figure 5.9 – Response I, Vertical Displacement and Velocity

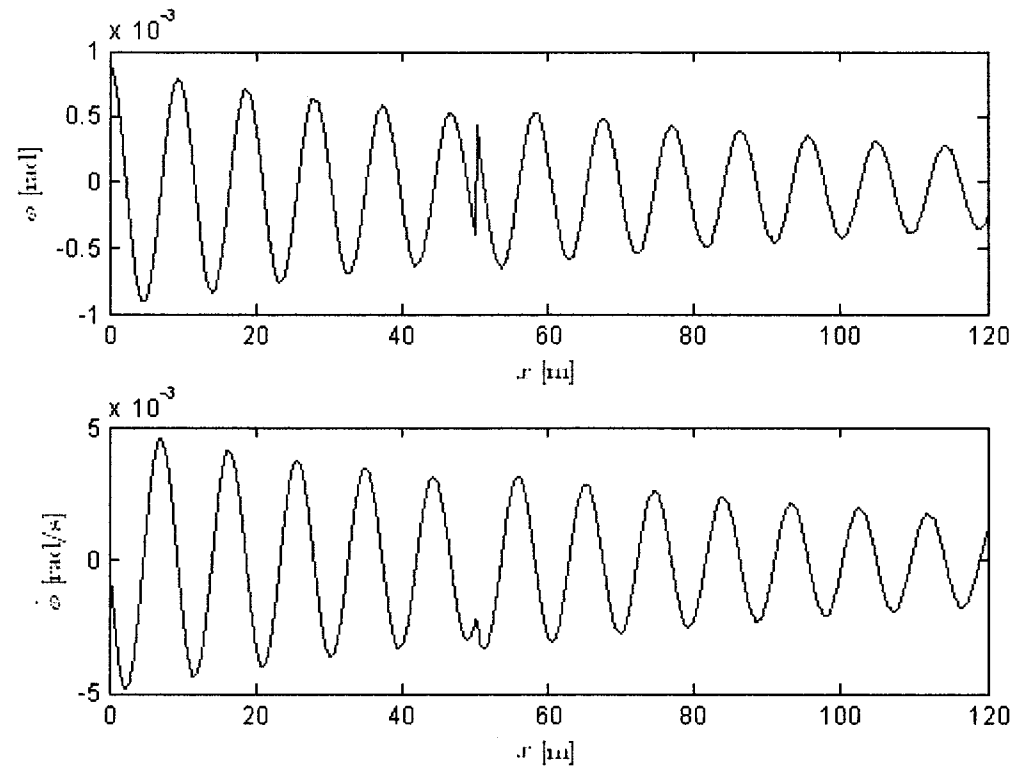

Figure 5.10 – Response I, Roll Angle and Rate

Figures 5.7 thought 5.10 depict Response I. From Figure 5.6 the lateral shift of 5 mm at 50 m is reflected in the change of the equilibrium position from 0 mm to -5 mm. Lateral velocity in Figure 5.8, yaw angle and yaw rate in Figure 5.9, all show discontinuity at 50 m. Figure 5.10, at 50 m, shows immediate increase or decrease in z displacement on both the left and right wheels as the track shifted. Due to this immediate disruption, a spike in vertical velocity occurs, as shown in the lower plot of Figure 5.9

5.4.2 Response II

Response II is conducted on a straight, perfectly level track. The wheelset travels at a constant velocity of 8 m/s. An initial condition of 12 mm lateral displacement is used to demonstrate the situation of a large, on the flange tread rolling condition. Initial lateral velocity, yaw and yaw rate are set to zero. Figures 5.11 through 5.15 depict the responses of the system.

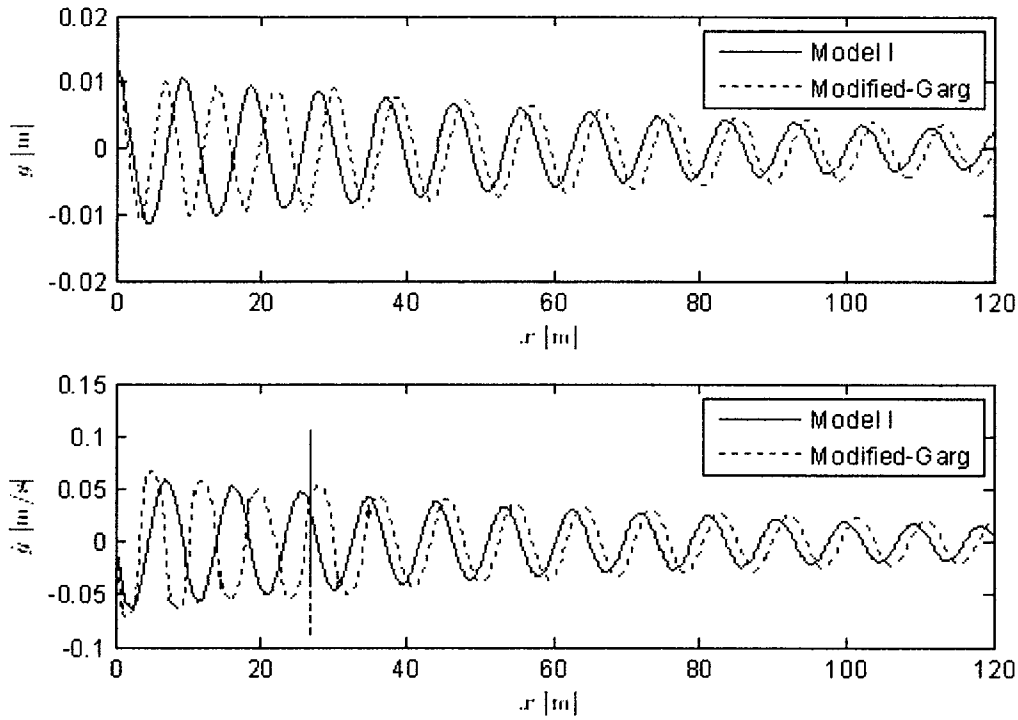

Figure 5.11 – Response II, Lateral Displacement and Velocity

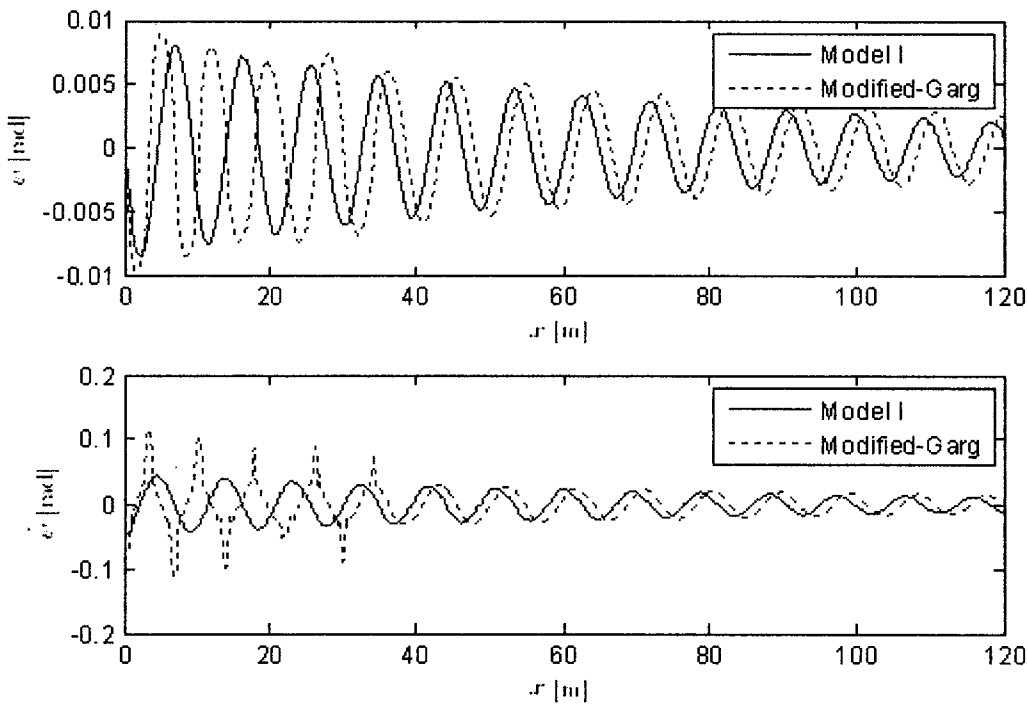

Figure 5.12 – Response II, Yaw Angle and Rate

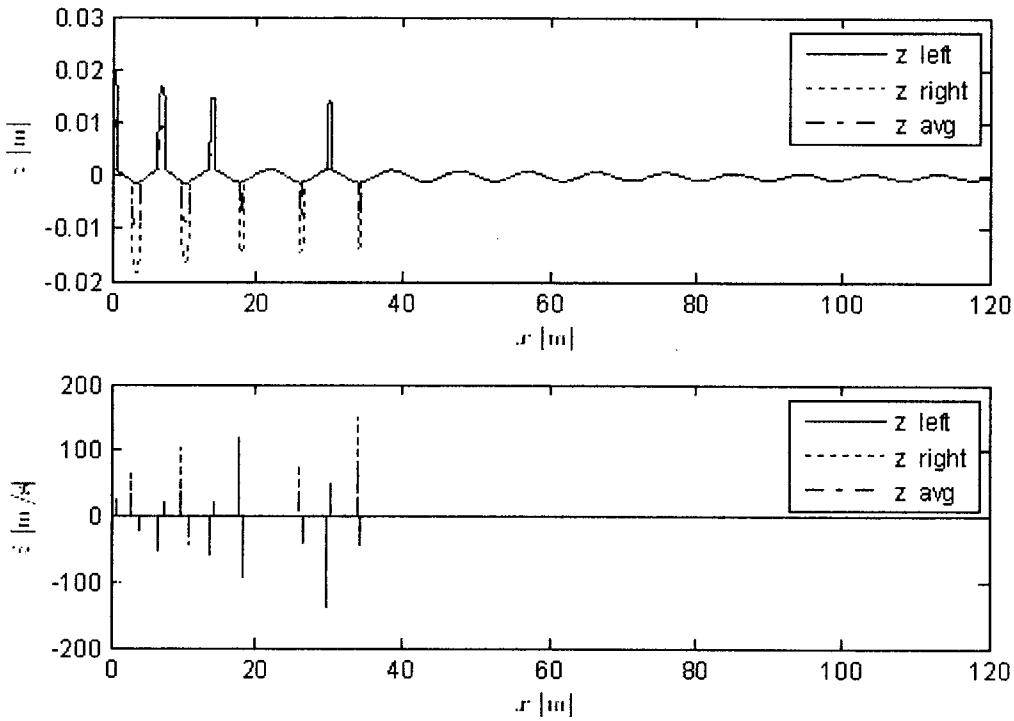

Figure 5.13 – Response II, Vertical Displacement and Velocity

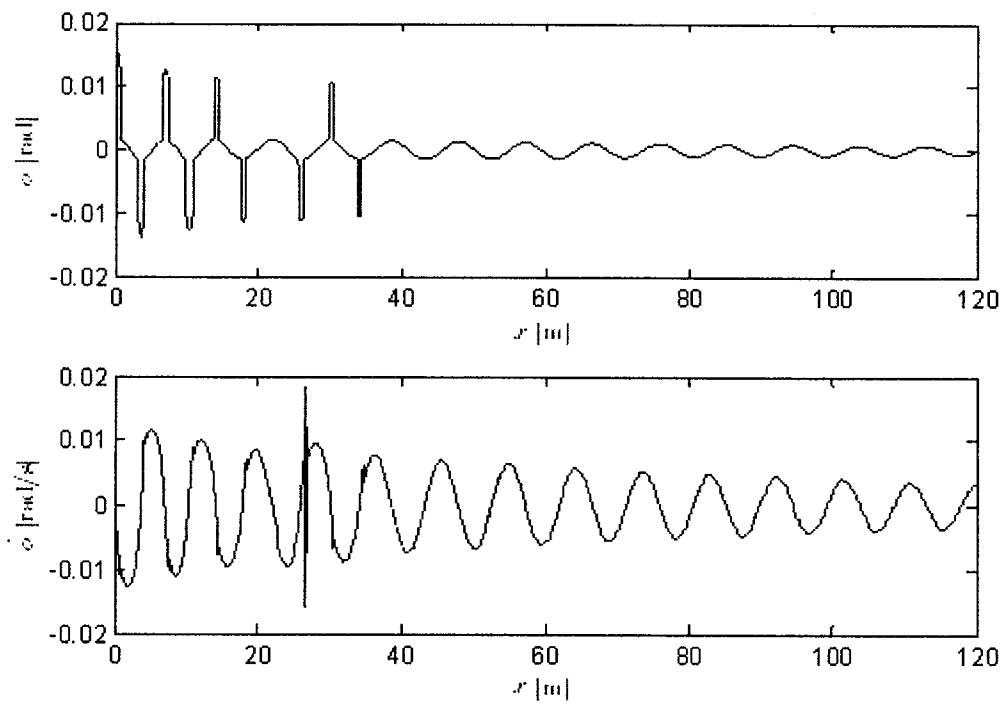

Figure 5.14 – Response II, Roll Angle and Rate

The larger difference in responses between Model I and the Modified-Garg model, so far depicted, seem caused by the difference in modeling flange contact and force. The initial conditions place the wheelset in a position where the left wheel is on the top of the flange. This position has a large left-right wheel radius difference, and therefore a large roll angle (0.015 rad in Figure 5.14 compared with 0.0009 rad in Figure 5.9).

Model I calculates the flange force, F_T by equation (4.27), in which the spring constant k_r is for a different but unspecified rail-wheel combination. The Modified-Garg model calculated the flange forces by considering multiple point contact.

As can be seen in Figure 5.11, the addition of the flange contact in the Modified-Garg model greatly effects the period of oscillation. Once the wheelset begins operating solely on the 7° treads ($-0.008 \geq y \geq 0.008$) the period of oscillation matches that of Model I. Shape distortions and spikes in the lateral velocity (Figure 5.11), the yaw rate (Figure 5.12) are due to impact with the flange against the rail. Spikes in the vertical displacement and velocity (Figure 5.13), and roll angle and rate (Figure 5.14) are all due to the large increase in rolling radii and the subsequent roll angle change from operating on the flange ($y \geq 0.008$ or $y \leq -0.008$).

5.5 Hunting

In 1821 George Stephenson observed and described a kinematic oscillation that would later be recognized as a wheelset hunting motion (see Figure 2.1) [5.4]. This hunting motion causes wear, inefficiency and safety concerns. It is of theoretical and practical importance to determine the velocity at which the oscillation will begin, otherwise known as the critical speed.

The critical speed can be determined by examining the wheelset's motion, since below the critical speed the motion will be damped out over time; beyond the critical speed, the motion will become unstable as depicted in Figure 5.16. This approach while not elegant provides an estimated critical speed.

Figure 5.15 and 5.16 illustrate the lateral displacement responses of Model I and the Modified-Garg model at forward velocities of $V = 11$ m/s through $V = 20$ m/s. It is seen that, at 15 m/s, Model I holds steady, and the Modified-Garg model starts to increase in oscillation amplitude. At 17 m/s, Model I also starts to increase in amplitude. The critical speed is reached 2 m/s slower with the Modified-Garg model which employs realistic wheel and rail profiles, and considers multiple point contact. Similarly, Models II and III have been represented in Figure 5.17 and 5.18. Model II shows a small increase in amplitude beginning at 17 m/s, while Model III begins to increase at around 21 m/s, a difference of 4 m/s. With critical speeds for the four models showing 15 (Modified-Garg), 17 (Models I and II), and 21 m/s (Model III), there is a large discrepancy among

the different approaches. It seems that the less restricted hence more accurate a model is, the lower the critical speed is predicted.

It should also be mentioned that this section is simply to demonstrate that the Modified-Garg model is able to capture the characteristics of the wheelset's motion below, at and beyond the critical speed. Critical speed can be more accurately and effectively determined by methods such as bifurcation [5.5] and limit cycle [5.6], for instance.

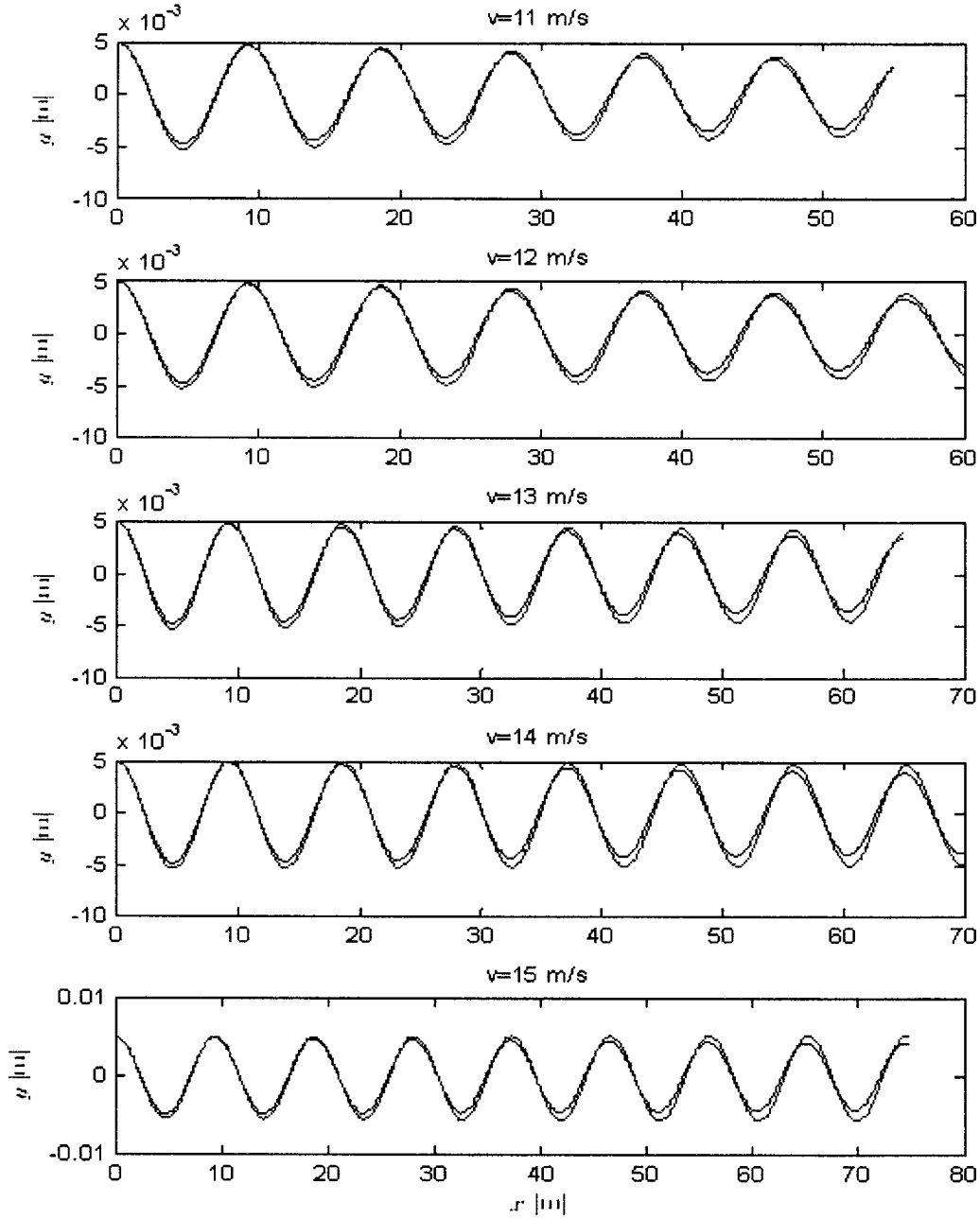

Figure 5.15 – Hunting, Part A

(Blue – Model I, Green – Modified-Garg)

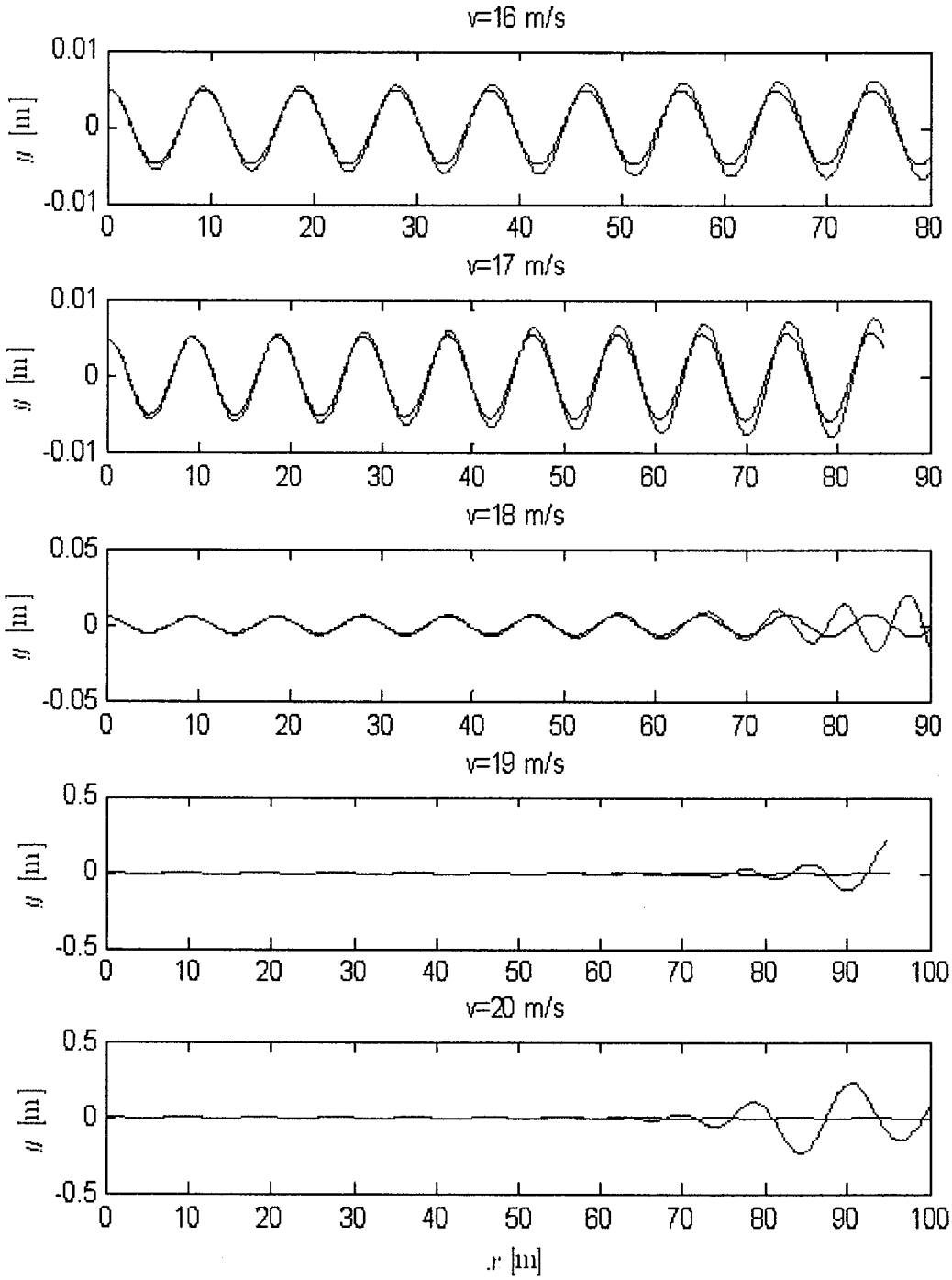

Figure 5.16 – Hunting, Part B

(Blue – Model I, Green – Modified-Garg)

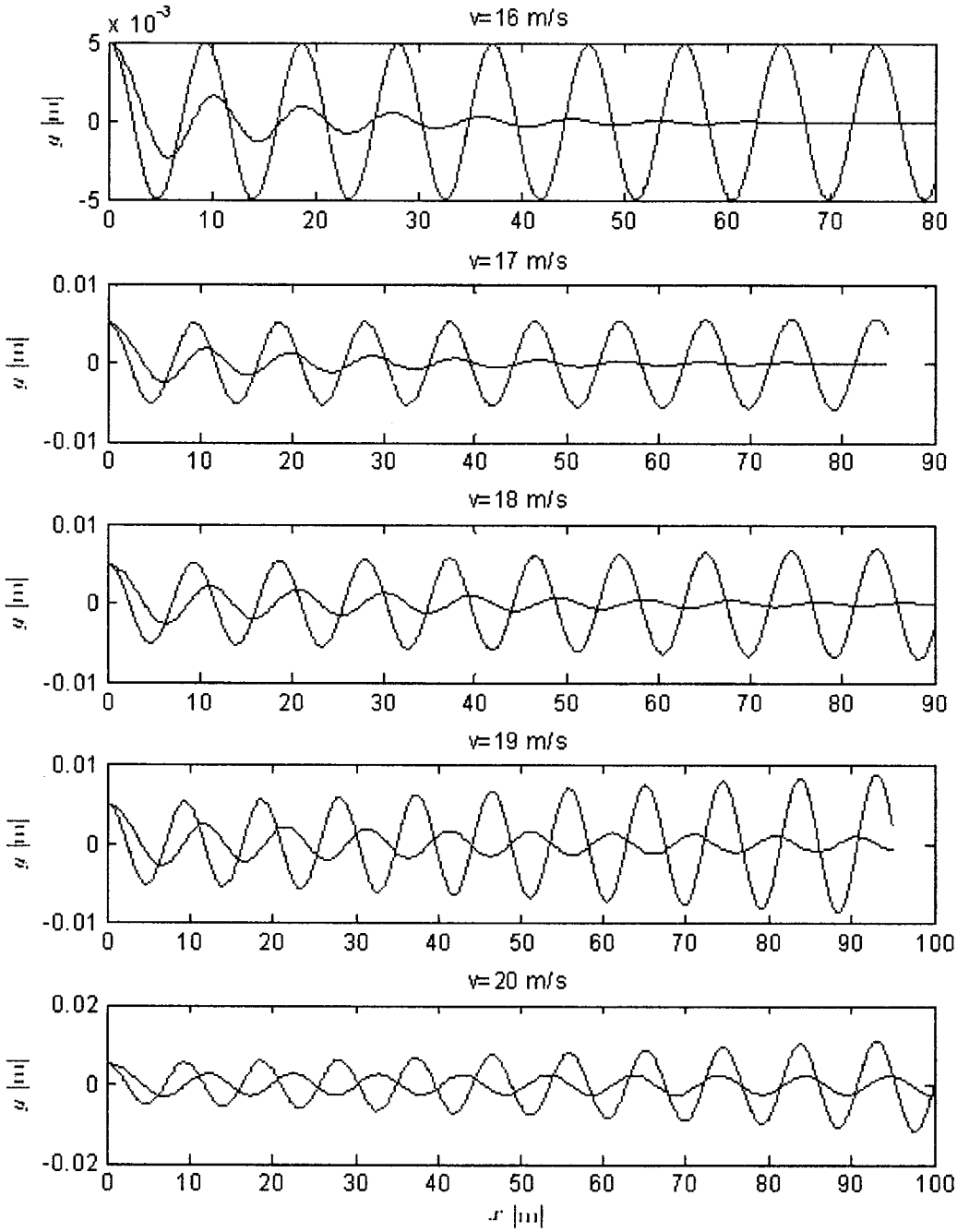

Figure 5.17 – Hunting, Part C

(Blue – Model II, Green – Model III)

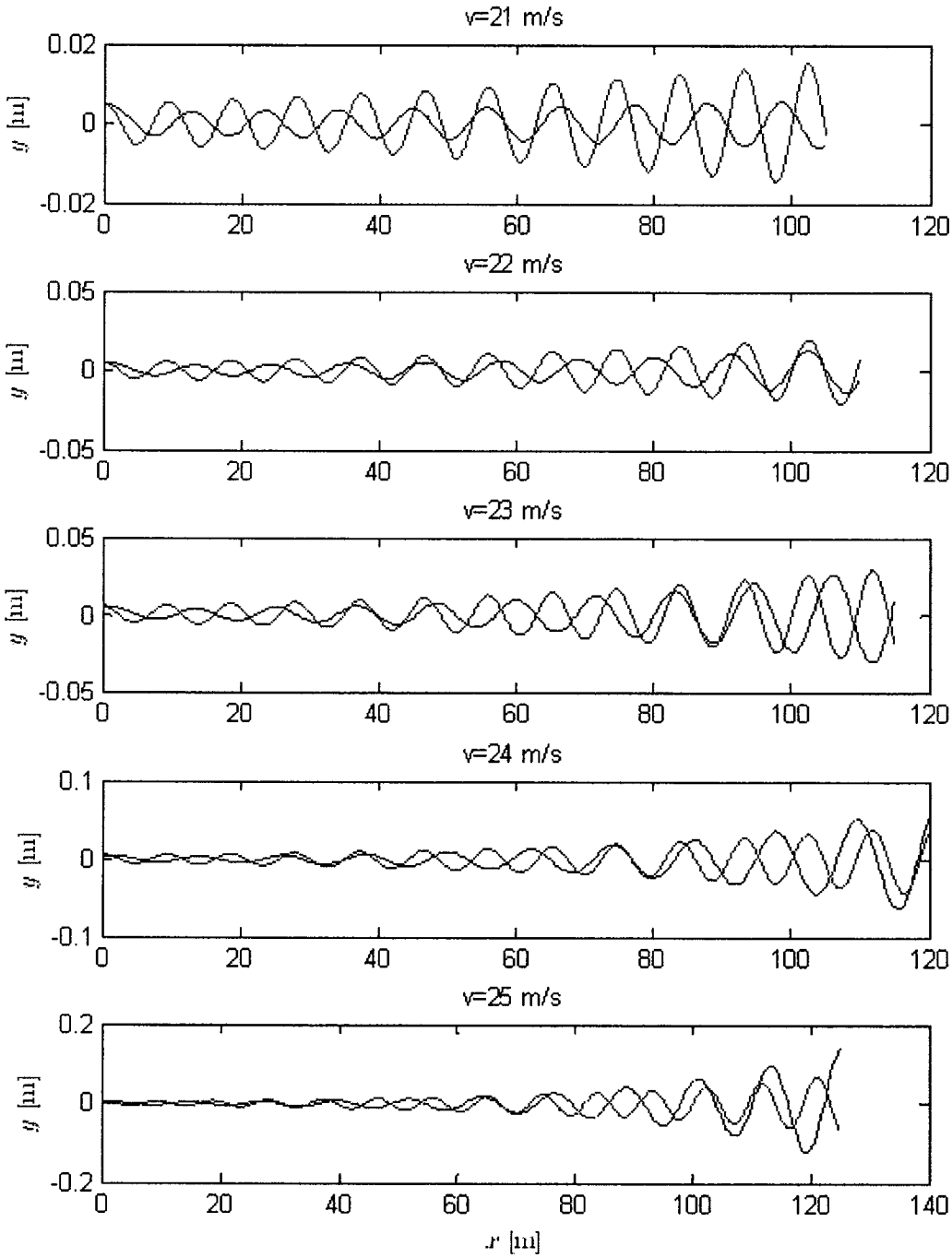

Figure 5.18 – Hunting, Part D

(Blue – Model II, Green – Model III)

5.6 Control

In terms of control, this thesis focuses on mechanical passive control. The Modified-Garg model and Model I both make use of two springs; a yaw spring (k_ψ) and a lateral spring (k_y). It is found that k_ψ yields greater effect on the system. Figure 5.19 depicts the lateral displacements over a wide range of k_ψ. Initial conditions include a 5 mm lateral shift, while lateral velocity, yaw angle, and yaw rate are set to zero. Longitudinal velocity is 8 m/s and constant. It is seen that, with small k_ψ ($\leq$ 150000 Nm^{-1}, say), the response does not dampen down, or dampens down very slowly. Damped response, however, is achievable with the use of higher k_ψ. The distance for the system to settle to 5% of the original displacement is found to be, 35.18 m, 17.42 m, and 9.27 m with the yaw spring taking values of $k_\psi = 15\text{x}10^5 Nm^{-1}$, $k_\psi = 30\text{x}10^5 Nm^{-1}$ and $k_\psi = 45\text{x}10^5 Nm^{-1}$ respectively. It should be noted that, in the above calculations, the system is assumed operating without viscous dampers, but does make use of creep forces which apply a damping effect.

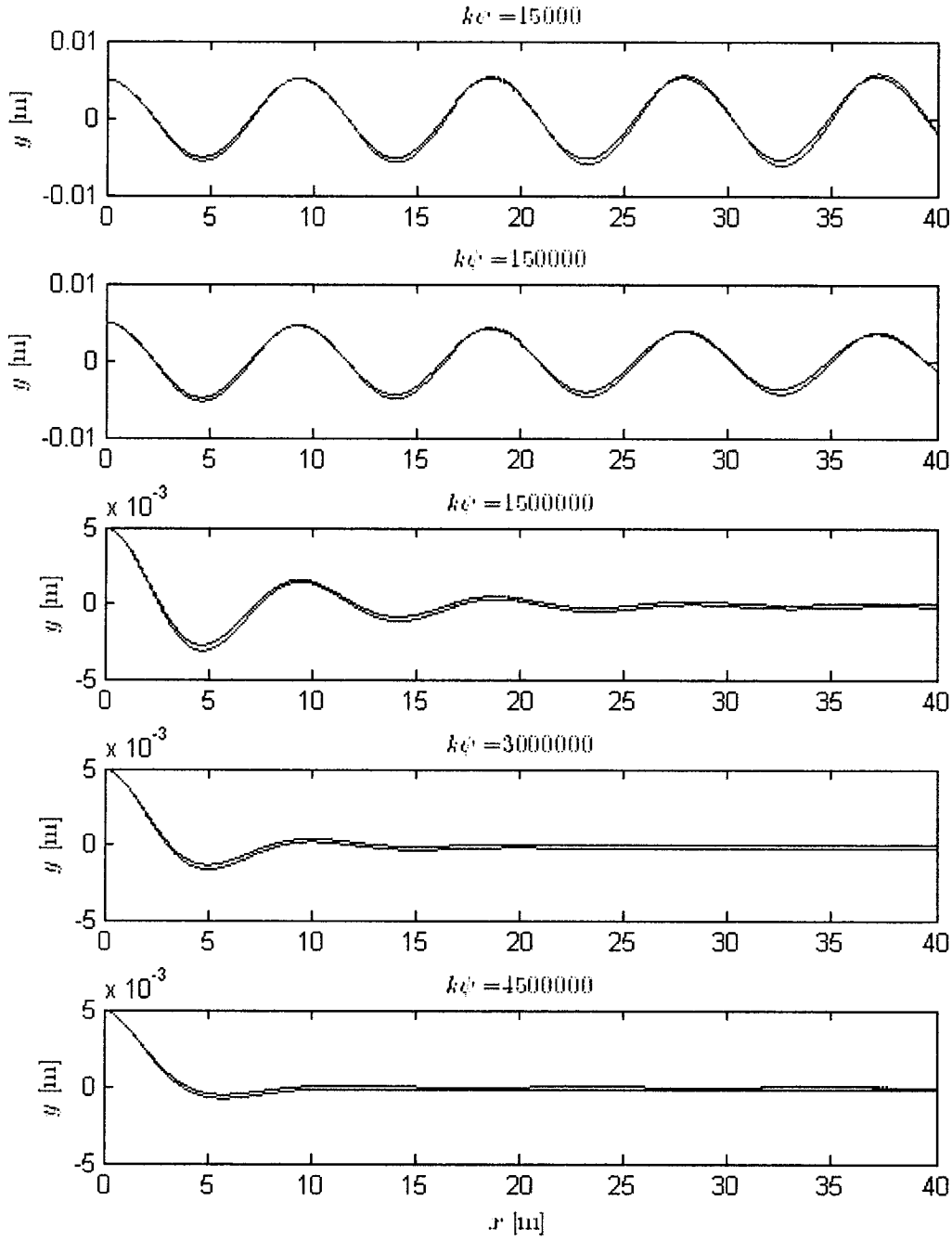

Figure 5.19 - k_ψ Variation on Lateral Displacement

(Blue – Model I, Green – Modified-Garg)

5.7 Conclusion

The Modified-Garg model incorporated realistic wheel and rail profiles. It calculated for normal forces at every time step and accepted both small and large angles. It used track-dependant creep forces (Section 4.2.2), calculated normal forces, and positions of contact points at every step. Contact conditions included one-point on the tread or on the flange, and two-point (flange and tread). Under normal operating conditions with single point contact taking place on the tread, the Modified-Garg model performed as well as Model I. The Modified-Garg model was able to capture behaviors such as wheel flange impacting upon rail, which Model I failed to do. The Modified-Garg model also calculated a lower critical speed than the three models presented in Chapter 4.

Chapter 6 – Conclusions and Recommendations for Future Work

This thesis presented the theories and numerical simulations in regard to the behaviour of a single-axle railway wheelset commonly used in cargo rail cars. Specifically, creep forces, dynamic models, real wheel-rail profiles, and multiple point contact were investigated.

One of the most important aspects of wheel-rail interactions is the creep force. Creep force results from the relative motion between the wheel and rail. The extent of such relative motion is measured by creepage, which is defined as the difference between ideal, or pure rolling, where the velocities of the wheel and rail relate to one another are equal, and the deviation of such. Creep is an important design factor in relation to rail transport safety and efficiency as well as wheel and rail longevity.

Calculation of the dynamic creep forces was completed with a nine-step process and benchmarked against Polach and Kalker. The Polach benchmarking tested three sets of creepage combinations proposed by Polach. In this test, a total of fifteen cases were tested. The creep forces were then plotted with respect to specific track cases and compared with multiple theories including Kalker's FASTSIM results. The relative accuracy and computational efficiency amongst the theories were determined. The Polach theory was found to satisfactorily capture and represent the dynamic responses of the wheelset.

Three dynamic models were presented and compared. Model I utilized dynamic creep forces, additional penetrations at wheel-rail contact points and the corresponding dynamic normal forces. Model II used static creep forces which are calculated by the Johnson and Vermeulen theory, while Model III used pre-calculated creep force coefficients. These models were tested under specific track conditions from the Manchester Benchmarks' Track Case 2 (TC2). These models were compared in the response, the time to calculate and the flexibility of the model to withstand parameter variations. The responses from Models I and II verified the nine-step process of determining dynamic creep forces and moment. Model II was limited to small roll and yaw, and Model III was limited to small angle situations due to the use of the Kalker theory. On the other hand, Model I was not subject to such limitations. It did assume the theoretically possible conical wheel and knife-edged rail.

In Chapter 5, real wheel and rail profiles were then introduced to replace the coned wheel and knife-edge rail assumption. This model made neither small angle assumptions nor normal force assumptions. Contact conditions included one-point contact, at either the tread or the flange, as well as two-point tread-flange contact. This model was again tested with TC2 and a large lateral disturbance. Under normal operating conditions with single point contact taking place on the tread, the Modified-Garg model performed as well as Model I. The Modified-Garg model also captured behaviors such as the wheel flange impacting upon rail, which Model I failed to do. The Modified-Garg model proved to be the most accurate model over the varying conditions. In particular, flange contact is a very important characteristic in railway dynamics as it causes wear, unbalanced

movement, and possible derailment. The ability of a model to capture flange contact is therefore very desirable.

Hunting, a side-to-side movement at specific velocities, was investigated by examining responses at the velocities. The Modified-Garg model predicted a critical speed lower than the other three models (15 m/s versus 17 or 21 m/s).

Finally, in terms of control, this thesis focused on mechanical passive control. It was found that k_{ψ} yielded the greatest effect on the system. Damped response, however, was achievable with the use of higher k_{ψ}. The distance for the system to settle to 5% of the original displacement was found to be, 35.18m, 17.42m, and 9.27m with the yaw spring taking values of $k_{\psi} = 15\text{x}10^{5} Nm^{-1}$, $k_{\psi} = 30\text{x}10^{5} Nm^{-1}$ and $k_{\psi} = 45\text{x}10^{5} Nm^{-1}$ respectively. It should be noted that the system is assumed operated without viscous dampers, but did make use of creep forces which apply a damping effect.

Recommendations for future work include:

(1) to extend the research to two-axle wheelsets, and subsequently to the assembly of wheelsets, trucks, and car bodies.

(2) to investigate additional mechanical damping in order to provide greater mechanical control.

(3) to investigate wheel and rail wear, and the effect on the dynamics from such.

Appendix A – Track Transformation Matrix

The following details the derivation of the transformation matrix for TC2, or A^{tc} in equation (4.17b). First, the track is treated as a curve with time t as the parameter. Coordinates of the curve at any given time t are,

$$x = Vt$$

$$y = \begin{cases} 0 & x \le 50 \\ p(x-50) & 50 < x \le 50.1 \\ 0.1p & x > 50.1 \end{cases}$$

$$z = 0$$

where p is,

$$p = \frac{0.005}{0.1}$$

The velocities are given as,

$$\dot{x} = V$$

$$\dot{y} = \begin{cases} 0 & x \le 50 \\ pV & 50 < x \le 50.1 \\ 0 & x > 50.1 \end{cases}$$

$$\dot{z} = 0$$

Lastly, the accelerations are given,

$$\ddot{x} = \ddot{y} = \ddot{z} = 0$$

In vector form, position, velocity, and acceleration vectors at t are,

$$\mathbf{r} = x\mathbf{i} + y\mathbf{j} + z\mathbf{k}$$
$$\dot{\mathbf{r}} = \dot{x}\mathbf{i} + \dot{y}\mathbf{j} + \dot{z}\mathbf{k}$$
$$\ddot{\mathbf{r}} = \ddot{x}\mathbf{i} + \ddot{y}\mathbf{j} + \ddot{z}\mathbf{k}$$

The tangent vector is then,

$$\mathbf{T} = \frac{\dot{\mathbf{r}}}{|\dot{\mathbf{r}}|} = \begin{cases} \begin{bmatrix} 1 & 0 & 0 \end{bmatrix}^T & x \le 50,\ x > 50.1 \\ \frac{1}{\sqrt{1+p^2}} \begin{bmatrix} 1 & p & 0 \end{bmatrix}^T & \text{otherwise} \end{cases}$$

The binormal vector is,

$$\mathbf{B} = \begin{bmatrix} 0 & 0 & 1 \end{bmatrix}^T$$

And the normal vector is,

$$\mathbf{N} = \mathbf{B} \times \mathbf{T} = \begin{cases} \begin{bmatrix} 0 & 1 & 0 \end{bmatrix}^T & x \le 50,\ x > 50.1 \\ \frac{1}{\sqrt{1+p^2}} \begin{bmatrix} -p & 1 & 0 \end{bmatrix}^T & \text{otherwise} \end{cases}$$

Therefore the transformation matrix is,

$$A^{tc} = \begin{bmatrix} \mathbf{T} & \mathbf{N} & \mathbf{B} \end{bmatrix} = \begin{cases} \begin{bmatrix} 1 & 0 & 0 \\ 0 & 1 & 0 \\ 0 & 0 & 1 \end{bmatrix} & x \le 50,\ x > 50.1 \\ \begin{bmatrix} \frac{1}{\sqrt{1+p^2}} & \frac{-p}{\sqrt{1+p^2}} & 0 \\ \frac{p}{\sqrt{1+p^2}} & \frac{1}{\sqrt{1+p^2}} & 0 \\ 0 & 0 & 1 \end{bmatrix} & \text{otherwise} \end{cases}$$

The above expression can be written in a compact form by defining $\alpha = \frac{dy}{dx}$, such that,

$$A^{tc} = \begin{bmatrix} \cos\alpha & -\sin\alpha & 0 \\ \sin\alpha & \cos\alpha & 0 \\ 0 & 0 & 1 \end{bmatrix}$$

References

[1.1] De Pater, A. D., The Approximate Determination of the Hunting Movement of a Railway Vehicle by Aid of the Method of Krylov and Bogoljubow, in *Proccedings of the 10th International Congress of Applied Mechanics*, Stresa, Applied Science Resource, **10**, 1960.

[1.2] Wickens, A. H., The Dynamic Stability of Railway Vehicle Wheelsets and Bogies having Profiled Wheels, *International Journal of Solids and Structures*, **I**(3), 319-341, 1965.

[1.3] Kalker, J. J., *Simplified Theory of Rolling Contact*, Progress Report, Delft University of Technology, Delft, The Netherlands, 1973.

[2.1] Anderson, R. J., Elkins, J. A., Brickle, B. V., Rail Vehicle Dynamics for the 21st Century, in *Mechanics for a New Millennium*, pp. 113-126, Kluwer Academic Publishers, The Netherlands, 2001.

[2.2] Shabana, A. A., Sany, J. R., A Survey of Rail Vehicle Simulations and Flexible Multibody Dynamics, *Nonlinear Dynamics*, **26**, 179-210, 2001.

[2.3] Garg, V. K., Dukkipati, R.V., *Dynamics of Railway Vehicle Systems*, Academic Press, Toronto, Canada, 1984.

[2.4] Handoko, Y. A., *Investigation of the Dynamics of Railway Bogies Subjected to Traction / Braking Torque*, Ph.D. Thesis, Central Queensland University, Australia, 2006.

[2.5] Kalker, J.J., *On the Rolling Contact of Two Elastic Bodies in the Presence of Dry Friction*, Ph.D. Thesis, Delft University of Technology, Delft, The Netherlands, 1967.

[2.6] Kalker, J.J., *Three-dimensional elastic bodies in rolling contact*, Kluwer Academic Publishers, Dordecht/Boston/London, 1990.

[2.7] Kalker, J. J., *User's Manual of the Fortran IV Program CONTACT*, Report Department Mathematics and Infomatics, Delft University of Technology, The Netherlands, 1982.

[2.8] Kalker, J.J., The Tangential Force Transmitted by Two Elastic Bodies Rolling Over Each Other with Pure Creepage, *Wear II*, 421-430, 1968.

[2.9] Shabana, A. A., Zaazaa, K. E., Sugiyama, H., *Railroad Vehicle Dynamics, A Computational Approach*, CRC Press, Boca Raton, U.S.A., 2008.

[2.10] Kalker, J. J., *Simplified Theory of Rolling Contact*, Progress Report, Delft University of Technology, Delft, The Netherlands, 1973.

[2.11] Kalker, J. J., Fast Algorithm for the Simplified Theory of Rolling Contact, *Vehicle System Dynamics,* **11**(1), 1-13, 1982.

[2.12] Polach, O., A Fast Wheel-Rail Forces Calculation Computer Code, *Vehicle System Dynamics*, **33**(supplement), 728-739, 1999.

[2.13] Pombo, J.C., Ambrosio, J. A. C., Application of a Wheel-rail Contact Model to Railway Dynamics in Small Radius Curved Tracks, *Multibody System Dynamics*, **19**, 91-114, 2008.

[2.14] Lankarani, H. M., Nikravesh, P. E., A Contact Force Model with Hysteresis Damping for Impact Analysis in Multibody Systems, *ASME Journal of Mechanical Design*, **112**, 369-376, 1990.

[2.15] Lankarani, H. M., Nikravesh, P. E., Continuous Contact Force Models for Impact Analysis in Multibody Systems, *Nonlinear Dynamics*, **5**, 193-207, 1994.

[2.16] Mohan, A., Ahmadian, M., Nonlinear Investigation of the Effect of Primary Suspension on the Hunting Stability of a Rail Wheelset, in *Proceedings of the 2004 ASME/IEEE Joint Rail Conference*, Maryland, U.S.A., pp. 53-61, 2004.

[2.17] De Pater, A. D., The Approximate Determination of the Hunting Movement of a Railway Vehicle by Aid of the Method of Krylov and Bogoljubow, in *Proccedings of the 10^{th} International Congress of Applied Mechanics*, Stresa, Applied Science Resource, **10**, 1960.

[2.18] Wickens, A. H., The Dynamic Stability of Railway Vehicle Wheelsets and Bogies having Profiled Wheels, *International Journal of Solids and Structures*, **I**(3), 319-341, 1965.

[2.19] Knudsen, C., Feldberf, R., Jaschinski, A., Non-Linear Dynamic Phenomena in the Behaviour of a Railway Wheelset Model, *Nonlinear Dynamics*, **2**, 389-404, 1991.

[2.20] Knudsen, C., Slivsgaard, E., Rose, M., True, H., Feldberg, R., Dynamics of a Model of a Railway Wheelset, *Nonlinear Dynamics*, **6**, 215-236, 1994.

[2.21] Ahmadian, M., Yang, S., Hopf Bifurcation and Hunting Behaviour in a Rail Wheelset with Flange Contact, *Nonlinear Dynamics*, **15**(1), 15-30, 1998.

[3.1] Shabana, A. A., Zaazaa, K. E., Sugiyama, H., *Railroad Vehicle Dynamics, A Computational Approach*, CRC Press, Boca Raton, U.S.A., 2008.

[3.2] Kalker, J. J., *User's Manual of the Fortran IV Program CONTACT*, Report Department Mathematics and Infomatics, Delfit University of Technology, The Netherlands, 1982.

[3.3] Kalker, J. J., *Book of Tables for the Hertzian Creep-Force Law*, Report 96-61, Delft University of Technology, The Netherlands, 1996.

[3.4] Kalker, J. J., *Simplified Theory of Rolling Contact*, Progress Report, Delft University of Technology, Delft, The Netherlands, The Netherlands, 1973.

[3.5] Kalker, J. J., Fast Algorithm for the Simplified Theory of Rolling Contact, *Vehicle System Dynamics* **11**(1), 1-13, 1982.

[3.6] DataFit, Oakland Engineering, http://www.curvefitting.com.

[4.1] Polach, O., A Fast Wheel-Rail Forces Calculation Computer Code, *Vehicle System Dynamics*, **33**(supplement), 728-739, 1999.

[4.2] MATLAB, The Mathworks, http://www.mathworks.com.

[4.3] Iwnicki, S., The Results of the Manchester Benchmarks, *Vehicle System Dynamics*, **31**(supplement), 2-48, 1999.

[4.4] Nath, Y., Jayadev, K., Influence of Yaw Stiffness on the Nonlinear Dynamics of Railway Wheelset, *Communications in Nonlinear Science and Numerical Simulation*, **10**, 179-190, 2005.

[4.5] Garg, V. K., Dukkipati, R.V., *Dynamics of Railway Vehicle Systems*, Academic Press, Toronto, Canada, 1984.

[4.6] Petersen, D.E., Hoffmann, M. *Dry Friction and Impact Dynamics in Railway Vehicles*, M.Sc. Thesis, Technical University of Denmark, Lyngby, Denmark, 2003.

[5.1] American Public Transportation Association, http://www.apta.com.

[5.2] Mohan A. *Nonlinear Investigation of the Use of Controllable Primary Suspensions to Improve Hunting in Railway Vehicles*, M.Sc. Thesis, Virginia Polytechnic Institute and State University, Blacksburg, USA, 2003.

[5.3] Garg, V. K., Dukkipati, R.V., *Dynamics of Railway Vehicle Systems*, Academic Press, Toronto, Canada, 1984.

[5.4] Anderson, R. J., Elkins, J. A., Brickle, B. V., Rail Vehicle Dynamics for the 21st Century, in *Mechanics for a New Millennium*, pp. 113-126, Kluwer Academic Publishers, The Netherlands, 2001.

[5.5] Nath, Y., Jayadev, K., Influence of Yaw Stiffness on the Nonlinear Dynamics of Railway Wheelset, *Communications in Nonlinear Science and Numerical Simulation*, **10**, 179-190, 2005.

[5.6] Stichel, S., Limit Cycle Behavior and Chaotic Motions of Two-Axle Freight-Wagon with Friction Damping, *Multibody System Dynamics*, **8**, 243-255, 2002.